

Verification of a new radiation condition for two ships advancing in waves

Zhi-Ming Yuan

Department of Naval Architecture, Ocean and
Marine Engineering
University of Strathclyde, Glasgow, UK

Atila Incecik

Department of Naval Architecture, Ocean and
Marine Engineering
University of Strathclyde, Glasgow, UK

Day Alexander

Department of Naval Architecture, Ocean and Marine Engineering
University of Strathclyde, Glasgow, UK

Abstract: 3-D Rankine source method is used to investigate the hydrodynamic interactions between two ships arranged side by side with forward speed. The radiation condition is satisfied by using a modified Sommerfeld radiation condition which takes into account the Doppler shift of the scattered waves. This new radiation condition is applicable to a wide range of forward speeds, including very low forward speed problem where the parameter τ ($\tau = u\omega/g$) is smaller than 0.25. The numerical solution is evaluated by applying the present method to two pairs of models and compared with experimental data and Green function method. Through the comparison study, we verify the new radiation condition and examine the wave patterns for a full range of forward speeds. Discussions are highlighted on the effect of the radiation conditions.

Keywords: Hydrodynamic interaction; Rankine source method; Radiation condition; Wave pattern; Forward speed.

1 INTRODUCTION

Hydrodynamic interaction between two or more ships occurs in harbor area and waterways with dense shipping traffic as the vessels have to pass each other in close proximity; between tugs and vessels during escorting or maneuvering and berthing operations as well as during ship-to-ship operations for cargo transfers during oil and gas offloading operations. The behavior of two ships in waves with speed effect is of special concern to the Navy, that is, for underway replenishment, and for other commercial purposes.

Because of the hydrodynamic interactions, even relatively small wave can induce large motions of the smaller ship due to the nearness of the larger ship. When the ships are travelling with forward speed, the hydrodynamic interactions become more complicated. Fang and Kim [1] firstly took forward speed into consideration in ship-to-ship problem. They utilized a 2-D procedure, including the hydrodynamic interaction and an integral equation method, to predict the coupled motions between two ships advancing in oblique seas. They found that the roll motion was reduced while the ships were advancing. However, due to the 2-D assumptions, some deficiencies including the special treatment of the convective term still exist. Kashiwagi [2] used an unified theory to investigate the heave and pitch motions of a catamaran advancing in waves. Iwashita and Kataoka [3] used the 3D translating and pulsating Green-function method to analyse the hydrodynamic interaction between steady and unsteady flows for a catamaran. Chen and Fang [4] extended Fang's method [1] to 3-D. They used a 3-D Green function method to investigate the hydrodynamic problems between two moving ships in waves.

* Corresponding author at: Dep. of Naval Architecture, Ocean & Marine Engineering, University of Strathclyde, Henry Dyer Building, G4 0LZ, Glasgow, UK.
Tel: + 44 (0)141 548 2288. Fax: +44 (0)141 552 2879.
E-mail address: zhiming.yuan@strath.ac.uk

It was found that the hydrodynamic interactions calculated by 3-D method were more reasonable in the resonance region, where the responses were not so significant predicted by 2-D method. However, their method was only validated by model tests with zero speed. More rigorous validation should be made by further experiments. The first model test of two ships advancing in waves was conducted by Li [5]. Both ships were restrained in surge, sway and yaw, as well as the free motions in heave, roll and pitch. Taggart et al. [6] and Li [7] used that model test data to verify their numerical programs, which was based on 3-D Green function method. The numerical predictions and experiments showed that the presence of a larger ship could significantly influence the motions of a smaller ship in close proximity. But the numerical prediction of roll motion was not accurate. Another model test of two ships advancing in waves was conducted by Ronæss [8] at MARINTEK. The experiments were performed at different speeds and with different longitudinal distance between the ships. The numerical program based on unified theory was verified. It was found that heave and pitch motions could be predicted well while the roll motion was hard to predict due to the viscous effects. Ronæss's model test data was used by Xu and Faltinsen [9] to verify their numerical program based on 3-D Rankine source method. They applied an artificial numerical beach to satisfy the radiation condition. They found that the hydrodynamic peaks and spikes were related to the resonance modes in the water gap between the hulls. However, they also failed to predict the roll motion precisely. Recently, within the frame work of Green function, Xu and Dong [10] developed a 3-D translating-pulsating (3DTP) source method to calculate wave loads and free motions of two ships advancing in waves. Model tests were carried out to measure the wave loads and the free motions for a pair of side-by-side arranged ship models advancing with an identical speed in head regular waves. Both the experimental and the numerical predictions showed that hydrodynamic interaction effects on wave loads and free motions were significant. They also pointed out that the prediction accuracy of the 3DTP method was much better than that of 3DP, especially for peak values of the free motion responses.

We find that most of the publications on two ships with forward speed problem are based on Green function that satisfies the Kelvin free surface condition, as well as the radiation condition. It is an effective method for the zero speed problems, but if the vessel is travelling with forward speed, this method still has some limitations. Firstly, it could not account for the near-field flow condition. Although some researchers [11, 12] extended it to include the near-field free surface condition, the so-called irregular frequency still cannot be avoided. And it will bring singularity to the coefficient matrix equation. Secondly, it is impossible for the Green function to account for the effects of the steady flow on the unsteady potential. In the present study, the Rankine source approach will be applied, which uses a very simple Green function in the boundary integral formulation. This method requires the sources distributed not only on the body surface, but also on the free surface and control surface. Therefore, a flexible choice of free-surface conditions can be realized in these methods. The coupled behavior between steady and unsteady wave potential could be expressed in a direct formula. Meanwhile, the nonlinearity on the free surface could also be added in the boundary condition.

The Rankine source approach has been used by many investigators since it has been first proposed by Hess and Smith [13]. Investigators from MIT [14-16] applied the Rankine source approach to model steady and unsteady waves as a ship moves in waves. An analysis technique developed by Sclavounos and Nakos [14] for the propagation of gravity waves on a panelized free surface showed that a Rankine method could adequately predict the ship wave patterns and forces. Their work led to the development of a frequency-domain formulation for ship motions with a consistent linearization based upon the double body steady flow model which assumes small and moderate Froude numbers. Applications were reported by Nakos et al. [15]. This model was extended to the time domain by Kring [16] who also

proposed a physically rational set of Kutta conditions at a ship's transom stern. Recently, Gao et al. [17] developed a high-order Rankine panel method based on Non-Uniform Rational B-Spline (NURBS) to solve the 3-D radiation and diffraction problems with forward speed. Their results had very good agreement with the experimental data. However, there are still some limitations for the extensive use of the Rankine source approach. First of all, the Rankine source method requires much more panels which will considerably increase the computation time, especially when the matrix equation is full range matrix. However, the computation time will strongly depend on the numerical method and computer language. As the performance of computers increase rapidly, it only takes less than 1 minute to solve a $10^4 \times 10^4$ full range matrix using Matlab. Typically, the number of panels will be no more than 10,000. The computation time is acceptable in engineering applications. Besides, the Rankine source method requires a suitable radiation boundary condition to account for the scattered waves in current. A very popular radiation condition for the forward speed problem, which is so-called upstream radiation condition, was proposed by Nakos [18]. The free surface was truncated at some upstream points, and a quiescent boundary condition was imposed at these points to ensure the consistency of the upstream truncation of the free surface. Another method to deal with the radiation condition is to move the source points on the free surface at some distance downstream [19]. The results from these two methods show very good agreement with published experimental data when the parameter τ ($\tau = u\omega/g$) is greater than 0.25, since they are both based on the assumption that there is no scattered wave travelling ahead of the vessel. However, when the forward speed of the vessel is very low, τ will be smaller than 0.25. When this case occurs, the scattered waves could travel ahead of the vessel, and these traditional radiation conditions could no longer be valid. For ship-to-ship problem, the forward speed is usually limited to a low level for the safe operation. Therefore, a new extensive radiation condition should be proposed to deal with the very low forward speed problem. Das and Cheung [20, 21] provided an alternate solution to the boundary-value problem for forward speeds above and below the group velocity of the scattered waves. They corrected the Sommerfeld radiation condition by taking into account the Doppler shift of the scattered waves at the control surface that truncates the infinite fluid domain. They compared their results with the experimental data, and good agreement was achieved. They also computed the wave elevation on the free surface, and a reasonable wave pattern was obtained at $\tau < 0.25$ by using their new radiation condition. Yuan et al. [22] applied Das and Cheung's radiation condition to a Wigley III hull advancing in waves, and very good agreement had been achieved between their predictions and measurements.

In the present study, we will extend Das and Cheung's radiation condition to the ship-to-ship problem. A 3-D panel code based on Rankine source method will be developed to investigate the hydrodynamic interaction between two vessels arranged side by side with forward speed. The motion responses of both ships will be calculated and compared to Li's and Ronæss' experimental results. Discussions will be highlighted on the wave patterns at full range of forward speeds.

2 MATHEMATICAL FORMULATIONS OF THE POTENTIALS

2.1 COORDINATE SYSTEMS

The corresponding right-handed coordinate systems are shown in Fig. 1. The body coordinate systems $o_a-x_a y_a z_a$ and $o_b-x_b y_b z_b$ are fixed on Ship_a and Ship_b respectively with their origins on the mean free surface, coinciding with the corresponding centre of gravity (CoG) in respect to x and y coordinates when both of the ships are at their static equilibrium positions. o_a-z_a and o_b-z_b are both positive upward. The inertia coordinate system $o-xyz$ with origin located on the calm free surface coincides with $o_a-x_a y_a z_a$ when the ship has no unsteady motions. $O-XYZ$ is the earth-fixed coordinate system with its origin

located on the calm free surface and OZ axis positive upward. Three components of translation motions include surge (η_1^a and η_1^b , which are parallel to x -axis), sway (η_2^a and η_2^b , which are parallel to y -axis) and heave (η_3^a and η_3^b , which are parallel to z -axis). Another three rotational motion components are roll (η_4^a and η_4^b , which rotate around x -axis), pitch (η_5^a and η_5^b , which rotate around y -axis) and yaw (η_6^a and η_6^b , which rotate around z -axis). The incident wave direction is defined as the angle between the wave propagation direction and X -axis. $\beta=180^\circ$ corresponds to head sea; $\beta=90^\circ$ corresponds to beam sea. dt denotes the transverse distance between two ships while dl is the longitudinal distance. u_0 is the forward speed.

In the computation, the motions and forces of Ship-a and Ship-b are concerted to the local coordinate system in which the origin is at the centre of gravity of each ship.

2.2 DIFFRACTION WAVE POTENTIAL

It is assumed that the surrounding fluid is inviscid and incompressible, and that the motion is irrotational, the total velocity potential exists which satisfies the Laplace equation in the whole fluid domain. Let t denote time and $\vec{\mathbf{x}} = (x, y, z)$ the position vector. A complex velocity potential provides a description of the flow as

$$\begin{aligned} \psi(\vec{\mathbf{x}}, t) = & u_0 [\varphi_s(\vec{\mathbf{x}}) - x] + \text{Re} \sum_{j=1}^6 [\eta_j^a \varphi_j^a(\vec{\mathbf{x}}) e^{-i\omega_e t} + \eta_j^b \varphi_j^b(\vec{\mathbf{x}}) e^{-i\omega_e t}] \\ & + \text{Re}[\eta_0 \varphi_0(\vec{\mathbf{x}}) e^{-i\omega_e t}] + \text{Re}[\eta_7 \varphi_7(\vec{\mathbf{x}}) e^{-i\omega_e t}], \quad j=1, 2, \dots, 6 \end{aligned} \quad (1)$$

where φ_s is the steady potential and it is neglected in the present study; φ_j^a and φ_j^b ($j=1, 2, \dots, 6$) are the spatial radiation potential in six degrees of freedom corresponding to the oscillations of Ship_a and Ship_b respectively and η_j ($j=1, 2, \dots, 6$) is the corresponding motion amplitude (η_1 , surge; η_2 , sway; η_3 , heave; η_4 , roll; η_5 , pitch; η_6 , yaw); $\eta_7 = \eta_0$ is the incident wave amplitude; φ_7 is the spatial diffraction potential; φ_0 is the spatial incident wave potential and ω_e is the encounter frequency. Generally, the body boundary conditions can be treated separately by the diffraction and radiation problem as follows:

1) Body boundary conditions for the diffraction problem:

$$\frac{\partial \varphi_7}{\partial n} = -\frac{\partial \varphi_0}{\partial n} \Big|_{S_a} \quad (2)$$

$$\frac{\partial \varphi_7}{\partial n} = -\frac{\partial \varphi_0}{\partial n} \Big|_{S_b} \quad (3)$$

2) Body boundary conditions for the radiation problem (Ship_a is oscillating while Ship_b is fixed):

$$\frac{\partial \varphi_j^a}{\partial n} = -i\omega_e n_j^a + u_0 m_j^a \Big|_{S_a} \quad (4)$$

$$\frac{\partial \varphi_j^a}{\partial n} = 0 \Big|_{S_b} \quad (5)$$

3) Body boundary conditions for the radiation problem (Ship_b is oscillating while Ship_a is fixed):

$$\frac{\partial \varphi_j^b}{\partial n} = -i\omega_e n_j^b + u_0 m_j^b \Big|_{s_b} \quad (6)$$

$$\frac{\partial \varphi_j^b}{\partial n} = 0 \Big|_{s_a} \quad (7)$$

where $\vec{n} = (n_1, n_2, n_3)$ is the unit normal vector directed inward on body surface. The m_j denotes the j -th component of the so-called m -term and for the slender vessels, it can be expressed by

$$\begin{aligned} (m_1, m_2, m_3) &= (0, 0, 0) \\ (m_4, m_5, m_6) &= (0, n_3, -n_2) \end{aligned} \quad (8)$$

The free surface boundary for both diffraction and radiation problem can be written as:

$$g \frac{\partial \varphi_j}{\partial z} - \omega_e^2 \varphi_j + 2i\omega_e u_0 \frac{\partial \varphi_j}{\partial x} + u_0^2 \frac{\partial^2 \varphi_j}{\partial x^2} = 0, \quad j = 1, 2, \dots, 7 \quad (9)$$

2.3 RADIATION CONDITION

Fig. 2 shows the Doppler Shift of the scattered wave field by a vessel travelling with constant forward speed u_0 in the positive x direction. When a vessel is moving from point B to point O , the traveling time should be $t=BO/u_0$. During this period of time, the vessel produces scattered waves all along BO (the first scattered wave should arise at point B). The control surface here is defined as a circle with its centroid on point O and its radius as BO . The velocity of the scattered wave is defined as c , $BO/u_0=BD/c$. According to the sine theorem, it can be easily transferred to

$$\frac{u_0}{c} = \frac{\sin \theta}{\sin \alpha} \quad (10)$$

The scattered wave velocity at D can be expressed as

$$c^2 = \frac{g}{k_s} \tanh k_s d \quad (11)$$

where ω_s is the angular frequency of the scattered waves from a fixed reference point given as

$$\omega_s = \omega_e + u_0 k_s \cos(\alpha - \theta) \quad (12)$$

$$\omega_s^2 = g k_s \tanh k_s d \quad (13)$$

in which k_s is the local wave number at any point on the free or control surface, and d is the water depth.

Combining Eqs. (10)-(13), we can obtain the following governing equation

$$\begin{aligned} & \cos^2 \left[\alpha - \sin^{-1} \left(\sqrt{\kappa} \sin \alpha / \sqrt{\tanh(\kappa / F_h^2)} \right) \right] \kappa^2 \\ & + \left\{ 2\tau \cos \left[\alpha - \sin^{-1} \left(\sqrt{\kappa} \sin \alpha / \sqrt{\tanh(\kappa / F_h^2)} \right) \right] - \tanh(\kappa / F_h^2) \right\} \kappa + \tau^2 = 0 \end{aligned} \quad (14)$$

At infinite water depth, $d \rightarrow \infty$, Eq. (14) can be reduced to

$$\cos^2 \left[\alpha - \sin^{-1} \left(\sqrt{\kappa} \sin \alpha \right) \right] \kappa^2 + \left\{ 2\tau \cos \left[\alpha - \sin^{-1} \left(\sqrt{\kappa} \sin \alpha \right) \right] - 1 \right\} \kappa + \tau^2 = 0 \quad (15)$$

where $\lambda_s = 2\pi / k_s$ is the local wave length, $\gamma = \lambda_s g / u_0^2$ is the dimensionless local wave length, $F_h = u_0 / \sqrt{gd}$ is the depth Froude number, $\kappa = 2\pi / \gamma$ is the dimensionless local wave number, and parameter $\tau = u_0 \omega_e / g$.

Let's discuss the dimensionless local wave length on x -axis. At $\alpha=0$ or π , $\sin^{-1}(\kappa \sin \alpha) = 0$ Eq. (15) becomes

$$\cos^2(\alpha) \kappa^2 + [2\tau \cos(\alpha) - 1] \kappa + \tau^2 = 0 \quad (16)$$

The solutions for Eq. (16) can be written as

$$\kappa = \frac{1 - 2\tau \cos \alpha \pm \sqrt{1 - 4\tau \cos \alpha}}{2 \cos^2 \alpha} \quad (17)$$

At $\alpha=0$ and $\tau < 0.25$, two solutions can be obtained from Eq.(17)

$$\gamma_1 = \frac{4\pi}{1 - 2\tau - \sqrt{1 - 4\tau}} \quad (18)$$

$$\gamma_2 = \frac{4\pi}{1 - 2\tau + \sqrt{1 - 4\tau}} \quad (19)$$

At $\alpha=\pi$, another group of two solutions can be obtained from Eq.(17)

$$\gamma_3 = \frac{4\pi}{1 + 2\tau - \sqrt{1 + 4\tau}} \quad (20)$$

$$\gamma_4 = \frac{4\pi}{1 + 2\tau + \sqrt{1 + 4\tau}} \quad (21)$$

These four solutions are shown in Fig. 3, which are identical to Becker's [23] results. It has been found by using the Green function method that at $\tau < 0.25$, there are three wave systems: one ring wave system and two Kelvin fan wave systems with different wedge angle [23, 24]. At $\tau > 0.25$, there are only two wave systems, one of which is the wave system formed by the outer fan waves. From Fig. 3, we find that at $\tau < 0.25$, there are four wave lengths in x -axis: γ_1 and γ_3 corresponds to the ring wave system, γ_2 and γ_4 corresponds to the inner and outer Kelvin fan wave systems respectively. It can also be found that at

$\tau > 0.25$, there are only two wave lengths in x-axis: γ_3 corresponds to the ring wave system and γ_4 corresponds to outer Kelvin fan wave system. We notice that the wave length of the ring wave system is much larger than that of Kelvin fan wave systems. In the numerical study, the free surface is usually truncated at $2L-3L$ upstream and downstream. This truncation length is in the same order as the length of the ring wave system. But for the Kelvin fan wave systems, this truncation length is much larger, and it can be regarded as infinity. In Rankine source method, if the truncation length is very large ($R \rightarrow \infty$), the radiation condition is not necessary since the numerical damping may dissipate the scattered waves before they reach the truncated control surface. And also, as demonstrated by Nakos [18], the short wave system carried insignificant energy. Therefore, in the present study, there is no radiation condition imposed to Kelvin fan wave systems. The radiation condition proposed in this paper is only applicable to solve the radiation and diffraction problem of the ring wave system. Therefore, the parameter k_s only refers to the local wave number of the ring wave system.

Let's define a point D , which is used to divide the control surface into two parts, S_{c1} and S_{c2} . If we cannot find the solutions from equation system (10)-(13), these points must be on the control surface S_{c2} . Otherwise, they are on S_{c1} . The critical θ at point D can be derived analytically. The scattered wave reaching point D is produced by the vessel at point B . Notice that $\alpha = 2\theta$, Eq. (10) can be written as

$$\frac{u_0}{c} = \frac{1}{2 \cos \theta} \quad (22)$$

Substituting Eqs. (11) and (22) into Eq. (12), we can obtain the following equation at infinite water depth

$$\frac{u_0 \omega_e}{g} = \frac{1}{4 \cos \theta} \quad (23)$$

Notice that $\tau = \frac{u_0 \omega_e}{g}$, Eq. (23) becomes

$$\cos \theta = \frac{1}{4\tau} \quad (24)$$

From Eq. (24), we find that

- i. $\tau < 0.25$, no solution can be found for the critical θ since the scattered waves can reach any points on the whole control surface. At this case, the scattered wave produced at point B should reach somewhere ahead of point A . Correspondingly, the wave group will travel ahead of the vessel.
- ii. $\tau = 0.25$, the critical rotated angle $\theta = 0$. At this case, the scattered wave produced at point B is propagating to point A . Correspondingly, the wave group is reaching point O .
- iii. $\tau > 0.25$, the critical θ can be found at point D . At this case, the control surface could divide into arc DB (S_{c1}) and arc DA (S_{c2}).

In the numerical calculation, the coordinates of any arbitrary point on the control surface are given, and then the unknowns θ and k_s could be obtained by solving the nonlinear equation system (10)-(13). The radiation condition is defined as two different equations on S_{c1} and S_{c2} independently,

$$\frac{\partial \varphi_j}{\partial n} - ik_s \varphi_j \cos \theta = 0 \quad (j=1, 2, \dots, 7) \text{ on } S_{c1} \quad (25)$$

$$\nabla \varphi_j = 0 \quad (j=1, 2, \dots, 7) \text{ on } S_{c2} \quad (26)$$

Eq. (25) is an updated Sommerfeld radiation condition with forward speed correction. If the forward speed is zero, $k_s=k$, $\theta=0$ and Eq. (25) could reduce to the Sommerfeld radiation condition as

$$\frac{\partial \varphi_j}{\partial n} - ik \varphi_j = 0 \quad (j=1, 2, \dots, 6) \text{ on } S_c \quad (27)$$

The radiation condition (25) and (26) can also be applied to ship-to-ship problem, as shown in Fig. 4. It is assumed that two ships are advancing in waves with the same forward speed. The transverse and longitudinal distances between two ships are dt and dl respectively. The inertia coordinate system is shown in Fig. 4 with its origin located on the central line between two ships. Fig. 5 is a numerical case of two oscillating sources advancing in the positive x direction. The free surface is truncated by a circle. To simplify the problem, only 40 nodes are distributed on the control surface (20 nodes on the upper half circle and 20 nodes on the lower half circle). Fig. 6 is the calculated local wave number and rotated angle respectively at $\tau=0.2$. The solutions of k_s and θ can be found at any nodes on the control surface, which illustrate that the scattered waves could reach any points on the truncated surface. Due to the Doppler Effect, the scattered waves upstream have shorter wavelengths. As a result, the local wave number upstream is greater than that downstream, which is shown in Fig. 6 (a). But the maximum values of rotated angle appear around $y=0$, and it decreases upstream and downstream gradually. It is very interesting to find that on the upper half circle, the rotated angle θ_a is close to zero at Node 1 and Node 19 while on the lower half circle, θ_b turns to be zero at Node 1 and Node 19. This is because these two nodes are almost on the trajectory of source **a** and source **b**, which can be shown in Fig. 5. At these points, the scattered wave direction is parallel to x axis and it will not be rotated at all. Since the origin of the control surface is located on the central line between two sources, the symmetry cannot be achieved about the trajectory of source **a** and source **b**. Therefore, the results on upper and lower half circle are different. The results of source **a** and source **b** are also not identical to each other. Fig. 7 is the calculated local wave number and rotated angle respectively at $\tau=0.6$. In numerical calculation, if there is no solution for equation system (10)-(13), the k_s and θ are labelled as 0. With regard to source **a**, the scattered waves can only propagate to Node 7 on the upper half circle, while Node 6 is the furthest point on the lower half circle. Ahead of these two nodes, there is no scatter wave and k_s and θ are labelled as 0. Since source **b** is located at some distance afterward, its scattered waves can only reach Node 5 on the upper half circle while Node 6 is the furthest point on the lower half circle. We also calculate k_s and θ at $\tau=0.4$. The critical nodes are shown in Fig. 5. It can be concluded that the quiescent region expands as the increase of τ , since the scattered waves are convected behind the sources. It can also be easily demonstrated that the truncation of free surface could be arbitrary (circular, rectangular or ellipse) and k_s and θ are only determined by the coordinates of the points on the control surface.

3 EQUATION OF MOTION

Once the unknown diffraction potential φ_7 and radiation potential φ_j are solved, the time-harmonic pressure can be obtained from Bernoulli's equation:

$$p_j = \rho \eta_j \left(i\omega_e \varphi_j + u_0 \frac{\partial \varphi_j}{\partial x} \right), \quad j=0, 1, \dots, 7 \quad (28)$$

where ρ is the fluid density. The hydrodynamic force produced by the oscillatory motions of the vessel in the six degrees of freedom can be derived from the radiation potentials as [25]

$$F_i^{Ra} = \sum_{j=1}^6 \iint_{S_a} p_j^a n_i dS \cdot (\eta_j^a + \eta_j^b) = \sum_{j=1}^6 \left[\omega_e^2 A_{ij}^{aa} + i\omega_e B_{ij}^{aa} \right] \eta_j^a + \sum_{j=1}^6 \left[\omega_e^2 A_{ij}^{ab} + i\omega_e B_{ij}^{ab} \right] \eta_j^b, \quad i=1, 2, \dots, 6 \quad (29)$$

$$F_i^{Rb} = \sum_{j=1}^6 \iint_{S_b} p_j^b n_i dS \cdot (\eta_j^a + \eta_j^b) = \sum_{j=1}^6 \left[\omega_e^2 A_{ij}^{ba} + i\omega_e B_{ij}^{ba} \right] \eta_j^a + \sum_{j=1}^6 \left[\omega_e^2 A_{ij}^{bb} + i\omega_e B_{ij}^{bb} \right] \eta_j^b, \quad i=1, 2, \dots, 6 \quad (30)$$

The added mass and damping can be expressed respectively as:

$$\begin{aligned} A_{ij}^{aa} &= -\frac{\rho}{\omega_e} \iint_{S_a} \left(\varphi_{ij}^a - \frac{u_0}{\omega_e} \frac{\partial \varphi_{Rj}^a}{\partial x} \right) n_i ds \\ A_{ij}^{ab} &= -\frac{\rho}{\omega_e} \iint_{S_a} \left(\varphi_{ij}^b - \frac{u_0}{\omega_e} \frac{\partial \varphi_{Rj}^b}{\partial x} \right) n_i ds \\ A_{ij}^{bb} &= -\frac{\rho}{\omega_e} \iint_{S_b} \left(\varphi_{ij}^b - \frac{u_0}{\omega_e} \frac{\partial \varphi_{Rj}^b}{\partial x} \right) n_i ds \\ A_{ij}^{ba} &= -\frac{\rho}{\omega_e} \iint_{S_b} \left(\varphi_{ij}^a - \frac{u_0}{\omega_e} \frac{\partial \varphi_{Rj}^a}{\partial x} \right) n_i ds \end{aligned} \quad (i=1, 2, \dots, 6; j=1, 2, \dots, 6) \quad (31)$$

$$\begin{aligned} B_{ij}^{aa} &= -\rho \iint_{S_a} \left(\varphi_{Rj}^a + \frac{u_0}{\omega_e} \frac{\partial \varphi_{ij}^a}{\partial x} \right) n_i ds \\ B_{ij}^{ab} &= -\rho \iint_{S_a} \left(\varphi_{Rj}^b + \frac{u_0}{\omega_e} \frac{\partial \varphi_{ij}^b}{\partial x} \right) n_i ds \\ B_{ij}^{bb} &= -\rho \iint_{S_b} \left(\varphi_{Rj}^b + \frac{u_0}{\omega_e} \frac{\partial \varphi_{ij}^b}{\partial x} \right) n_i ds \\ B_{ij}^{ba} &= -\rho \iint_{S_b} \left(\varphi_{Rj}^a + \frac{u_0}{\omega_e} \frac{\partial \varphi_{ij}^a}{\partial x} \right) n_i ds \end{aligned} \quad (i=1, 2, \dots, 6; j=1, 2, \dots, 6) \quad (32)$$

where A_{ij}^{aa} is the added mass of Ship_a in i -th mode which is induced by the motion of Ship_a in j -th mode; A_{ij}^{ab} is the added mass of Ship_a in i -th mode which is induced by the motion of Ship_b in j -th mode; A_{ij}^{ba} is the added mass of Ship_b in i -th mode which is induced by the motion of Ship_a in j -th mode;

mode; A_{ij}^{bb} is the added mass of Ship_b in i -th mode which is induced by the motion of Ship_b in j -th mode; B is the added damping and the definition the subscript is the same as that of added mass; φ_{Rj} is the real part of j -th potential, and φ_{Ij} is the imaginary part. The wave excitation force can be obtained by the integration of incident and diffraction pressure as

$$F_i^{Wa} = \iint_{S_a} (p_0 + p_7) n_i dS \quad (33)$$

$$F_i^{Wb} = \iint_{S_b} (p_0 + p_7) n_i dS \quad (34)$$

Applying Newton's second law, the 12 components of ship motions in the frequency domain can be obtained by solving the following equation system:

$$\sum_{j=1}^6 \left\{ \left[-\omega_e^2 (M_{ij}^a + A_{ij}^{aa}) + i\omega_e B_{ij}^{aa} + C_{ij}^a \right] \eta_j^a + \left[-\omega_e^2 A_{ij}^{ab} + i\omega_e B_{ij}^{ab} \right] \eta_j^b \right\} = F_i^{Wa}, \quad i=1, 2, \dots, 6 \quad (35)$$

$$\sum_{j=1}^6 \left\{ \left[-\omega_e^2 A_{ij}^{ba} + i\omega_e B_{ij}^{ba} \right] \eta_j^a + \left[-\omega_e^2 (M_{ij}^b + A_{ij}^{bb}) + i\omega_e B_{ij}^{bb} + C_{ij}^b \right] \eta_j^b \right\} = F_i^{Wb}, \quad i=1, 2, \dots, 6 \quad (36)$$

where M_{ij}^a and M_{ij}^b represent the generalized mass matrix for Ship_a and Ship_b; C_{ij}^a and C_{ij}^b represent the restoring matrix of Ship_a and Ship_b.

The standard matrix solution routine provides the complex amplitude of the oscillatory motions from Eqs. (35)-(36). The wave elevation on the free surface then can be obtained from the dynamic free surface boundary condition in the form

$$\zeta_j = \frac{i\omega_e}{g} (\eta_j^a \varphi_j^a + \eta_j^b \varphi_j^b) + \frac{1}{g} \nabla(\varphi_s - u_0 x) \cdot \nabla(\eta_j^a \varphi_j^a + \eta_j^b \varphi_j^b) = \zeta_{Rj} + i\zeta_{Ij}, \quad j=0, 1, \dots, 7 \quad (37)$$

where ζ_{Rj} is the the real part of j -th model, and ζ_{Ij} is the imaginary part.

4 NUMERICAL IMPLEMENTATION

In the numerical study, the boundary is divided into a number of quadrilateral panels with constant source density $\sigma(i)$ ($i=1,2,\dots,N$), where N is the panel number. The potential at the i th panel (the centroid coordinate can be denoted as (x_i, y_i, z_i)) induced by the j th panel (the centroid coordinate can be denoted as (x_j, y_j, z_j)) can be expressed by

$$\varphi_{i,j} = G_{i,j} \sigma_j, \quad i, j = 1, 2, \dots, N \quad (38)$$

where φ denotes the steady potential φ_s or the unsteady potential φ_j , $G_{i,j}$ is the Rankine-type Green function that satisfies the sea bed boundary condition through the method of mirror image

$$G_{i,j} = \frac{1}{\sqrt{(x_i - x_j)^2 + (y_i - y_j)^2 + (z_i - z_j)^2}} + \frac{1}{\sqrt{(x_i - x_j)^2 + (y_i - y_j)^2 + (z_i + 2d + z_j)^2}} \quad (39)$$

When the i th panel and the j th panel are close to each other, $G_{i,j}$ can be calculated with analytical formulas listed by Prins [26]. When the distance between the i th panel and the j th panel is large, these coefficients are calculated numerically.

The first derivatives of the potential are evaluated with analytical formulas for the first derivatives of the Rankine source shown in Hess and Smith [13].

Special attentions should be paid on the second derivatives of the potential on the free surface. Generally, the difference schemes can be divided in two classes: upwind difference schemes and central difference schemes. Although central difference schemes are supposed to be more accurate, the stabilizing properties of the upwind difference schemes are more desired in the forward speed problem [27]. Physically this can be explained by the fact that new information on the wave pattern mainly comes from the upstream side, especially at high speeds, whereas the downstream side only contains old information. The first-order upwind difference scheme for the second derivative of the potential to x can be written as follows

$$\varphi_{i,j}^{xx} = \frac{1}{\Delta x_j^2} [\varphi_{i,j+2} - 2\varphi_{i,j+1} + \varphi_{i,j}] \quad (40)$$

By substituting the first and second derivatives of the potential into the body-, free- and control-surface boundary conditions, the following set of linear equations for the values of the source density can be obtained

$$\sum_{j=1}^N P_{i,j} \sigma_j = Q_i, \quad i = 1, 2, \dots, N \quad (41)$$

For the constant panel method, the second derivatives of the potential can be expressed analytically [28]. However, we find that when the analytical expression is used, the condition number of the coefficient matrix $P_{i,j}$ is extremely large and the coefficient matrix tends to be an ill-conditioned matrix. The diagonal elements ($i=j$) is very large due to the factor that the field point is within the source panel. As a result, except the diffracted and radiated wave modes, some spurious wave modes can also be observed on the free surface, which could interfere with the physical waves and eventually destroy the credibility of the solution completely. This is a purely numerical phenomenon that firstly discussed by Longuet-Higgins and Cokelet [29]. They found that the saw-tooth like waves were superimposed on the physical waves such that the waves were zigzag alike if no preventive measure is taken. The general consensus on the cause of the problem is that there is high concentration of fluid particles with high speed in certain regions especially near the wave crests. The same phenomenon was also encountered by Xu and Yue [30] in their 3-D solution. A typical treatment to remove the saw-tooth instability is by introducing a low-pass numerical filter [29-31]. Although it can provide a smooth wave pattern, it is believed that this numerical filter can bring some influence to the real wave elevation. We find the difference scheme on the free surface boundary condition is the main reason for the spurious wave modes. Even without numerical filtering, the upstream difference scheme can obtain a smooth wave pattern. When the upwind difference scheme is used, the diagonal elements of the coefficient matrix can be restrained and as a result, the condition number decreases and the solution tends to be stable.

It should also be noticed that the singularity distribution does not have to be located on the free surface itself, it can also be located at a short distance above the free surface, as long as the collocation points, where the boundary condition has to be satisfied, stay on the free surface. In practice, a distance of maximal three times the longitudinal size of a panel is possible [27]. In the present study, the raised distance $\Delta z_i = \sqrt{S_i}$, where S_i is the area of the i th panel.

5 VALIDATIONS AND DISCUSSION

In realistic conditions, a ship cannot be considered as a point source and different parts of its hull usually produce several wave systems. Generally, only stern waves have magnitude comparable with that of bow waves. The diverging bow and stern waves may travel independently if the ship is long enough [32]. The longer waves and the shift of the origin downstream of the vessel require the replacement of the control surface further away to satisfy the point source assumption. However, Das and Cheung [21] carried out the convergence study and found that the present model apparently handled those phenomena well with constant panels and provided accurate results with a domain of reasonable dimensions and solution commonly used in ship and offshore platform design. In this paper, we will verify the present numerical program through two pairs of models. Model 1 is about a full scale supply ship and frigate model, and Li's model test results [7] will be used to verify the present numerical calculation. Model 2 is a tanker-LNG ship model in model scale, and Ronæss' experiments [8] will provide the motion responses for validation.

5.1 RESULTS OF MODEL 1

The main particulars of supply ship (Ship_a) and frigate (Ship_b) are shown in Table 1. The transverse and longitudinal distances between two ships are 52.702 *m* and 0 *m* respectively. A typical case is simulated here: head sea with forward speed of 6.18 *m/s* ($F_n=0.15$). To be consistent with the model tests condition, both ships are restrained in surge, sway and yaw while the motions in heave, roll and pitch are free. In order to make comparison, we also present the numerical results of two ships at zero forward speed. The computational domain is shown in Fig. 8. The free surface is truncated at L_a upstream, $2L_a$ downstream, L_a in the supply ship sideward and L_b in the frigate sideward. There are 378 panels on the body surface of supply ship, 5400 on free surface, 2432 on the control surface and 414 on the body surface of frigate.

Fig. 9 shows the response amplitudes of two ships in heave, roll and pitch motions. The comparisons with experimental data and Green function method [7] are also included. The numerical results calculated by the present 3-D Rankine source method generally agree with the experimental data. In order to investigate the speed effect, we also present the results of two ships without forward speed. It can be observed that the increase of the response amplitude operators with forward speed is considerable, especially for the smaller ship (Ship_b). Roll motion of Ship_a is obviously reduced due to the forward speed. But for Ship_b, the roll motion increases dramatically at $\lambda/L > 1$ due to the forward speed. In heave and pitch motions, there are also some discrepancies between the predictions and measurements, especially in the long wave case. There are two aspects to explain these discrepancies. The first reason should be the model test set-up. From the published work, only three model tests can be found on ship-to-ship with forward speed problem [5, 8, 33]. It was found that the model test set-up was very challenging, especially for the measurement of roll motion. The second reason is the numerical program. The present potential flow program is based on the linear assumption. It can be found in Fig. 9 that the greatest discrepancies between measured and predicted motions generally occur at long wave

length. In these conditions, the motions of Ship_b are very large, especially in roll motion. It violates the linear assumption. Even for the model test, as demonstrated by Li [6], the experiments could not be completed for the highest two wavelengths due to excessive motions of the Ship_b (roll amplitude exceeds 30 degrees). Furthermore, the hydrodynamic interactions between these two ships are also very important. The motions of the larger ship (Ship_a) could influence the motions of smaller ship (Ship_b) significantly. The large amplitude roll motion is coupled with the heave and pitch motions, which is different from the single ship problem. The unpredictable roll motion in long wave length could also influence the predictions of heave and pitch motions.

We also find the roll motions of both ships are significantly influenced by the roll damping coefficient. It is found that the damping in roll cannot be predicted well by the radiation component only [34]. The difficulty in predicting the roll motion arises from the nonlinear characteristics of roll due to the effect of fluid viscosity. In ship-to-ship problem, the roll motion is always remarkable due to the hydrodynamic interaction between two ships. The present potential flow theory is based on the assumption that the surrounding fluid is inviscid and it cannot predict the roll damping precisely. To complement the viscous component, an equivalent linear damping coefficient is applied in the present study. The non-dimensional roll damping coefficient, κ , is given by

$$\kappa = \frac{B_{44} + B_{44v}}{2\sqrt{(I_{44} + A_{44})C_{44}}} \quad (42)$$

where B_{44v} is the viscous damping. This damping coefficient is written as a fraction between the actual damping coefficient, $B_{44} + B_{44v}$, and the critical damping coefficient, $2\sqrt{(I_{44} + A_{44})C_{44}}$. Fig. 10 is the numerical results of roll motion amplitudes of two ships at different damping coefficients. We find that $\kappa_a=0.2$ and $\kappa_b=0.6$ agree with the experimental results better than other values. This is because the roll motion of Ship_a is relatively small, while the roll motion of Ship_b is extremely large. Correspondingly, the nonlinear viscous characteristics of roll motion of Ship_b are more obvious. A larger equivalent linear damping coefficient should be used in the numerical simulations.

5.2 RESULTS OF MODEL 2

The main particulars of tanker (Ship_a) and LNG (Ship_b) are shown in Table 2. The details of model test set-up is elaborated by Ronæss [8]. She analysed the bias sources and carried out comparative study. She found that the experimental set up corrections were necessary and in the present calculation, such corrections will be used, as shown in Table 3. The forced roll centre is taken to be 0.032 m below the mean water level for Ship_a and 0.104 m above the mean water level for Ship_b. To be consistent with the model tests condition, Ship_a is restrained in surge and sway while the motions in heave, roll, pitch and yaw are free; Ship_b is restrained in surge, sway and yaw while the other degrees of freedom are set free. A typical case is simulated here: head sea with forward speed of 0.912 m/s (Froude number $F_n = u_0 / \sqrt{gL_a} = 0.15$). The transverse and longitudinal distances between two ships are 1.25 m and 0.09 m respectively, which indicates that the longitudinal centre of these two ships are approximately the same. In order to make comparison, we also present the results of single ship with the same forward speed and two ships at zero forward speed. The computational domain is shown in Fig. 11. The free surface is truncated at 1.05 L_a upstream, 1.84 L_a downstream, 1.05 L_a in the tanker sideward and 1.3 L_b in the LNG ship sideward. There are 420 panels on the body surface of tanker, 9020 on free surface, 2464 on the control surface and 420 on the body surface of LNG ship.

5.2.1 MOTION RESPONSES

Fig. 12 is the response amplitudes of two ships. The comparisons with experimental data and unified theory are also included. The present results in heave and pitch motion of both ships generally have a satisfied agreement with those of experimental data. A noticeable discrepancy can be observed in Fig. 12 (a) and Fig. 12 (e) at $\lambda/L_a=1.2$ and $\lambda/L_a=1.3$, which corresponds to the resonant frequency of heave and pitch of Ship_a respectively. But the resonant frequency in the numerical calculation is around $\lambda/L_a=1$ for both heave and pitch of Ship_a. This difference is attributed to the trim suspensions in the model test set-up [8]. When it comes to roll, the present prediction, as well as Ronæss' [8] calculation, is not satisfactory. The main reason for the discrepancies is about the damping coefficient, which has been discussed previously in the validation of Model 1. According to Ronæss [8], the roll viscous damping of Ship_a is taken as $B_{44v}=2B_{44}$ for the forward speed case and $B_{44v}=B_{44}$ for the zero speed case. For Ship_b, it is taken as $B_{44v}=B_{44}$ for the forward speed case and $B_{44v}=4B_{44}$ for the zero speed case. The lift damping is another factor, which will increase when the roll centre is above the mean water level [35]. Besides, the measurement of roll motion in the model test is full of challenges. The devices used to measure the roll motion could bring additional friction and upward forces, as demonstrated by Ronæss [8]. We also include the results of a single ship with forward speed. From the comparison, we find that the hydrodynamic interaction has much greater influence on the motions of the smaller ship. For heave and pitch motions of the larger ship (Ship_a), the influence from the smaller ship (Ship_b) is not noticeable. But the hydrodynamic interaction is the essential reason that induces the roll motion for both ships. There is no roll motion in head sea condition for a single ship due to the symmetrical characteristic.

5.2.2 EFFECT OF RADIATION CONDITION

Fig. 13 shows the real part of diffracted and radiated waves of two ships with high forward speed. Fig. 14 shows the total wave elevation, which is non-dimensionalized by the incident wave amplitude η_0 . It is observed that the symmetrical characteristic of wave pattern produced by single ship has been modified in the presence of the other one. A V-shape region is clearly convected downstream. The diffracted waves from the two sides interact with those from the gap through a system of transverse waves and approach the downstream boundary at an oblique angle. The radiated waves propagate sideward independently and approach the downstream boundary parallel. No reflections can be found on the boundary, which indicates physically that the proposed radiation condition can ensure that the waves propagate away from the ship.

Fig. 15 and Fig. 16 compare the wave patterns with and without Doppler shift correction in the radiation condition. In order to make an intuitive comparison, we divide the whole free surface into two parts through the centre line of Ship_a: portside part and starboard part. The lower half of each figure shows the wave pattern with Sommerfeld radiation condition without forward speed correction in Eq. (27), while the radiation condition in the upper half accounts for the Doppler shift correction as given by Eq. (25). Since the parameter τ is smaller than 0.25, the scattered waves will propagate ahead of the vessel. It can be observed that if the new radiation condition associated with Doppler shift correction is used, the waves appear smooth and stable. But for the Sommerfeld radiation condition without forward speed correction, there are some distortions and reflections from the control surface. Theoretically, all scattered waves normal to the control surface must be out-going to avoid reflection. Since the Doppler shift results in rotation of the scattered waves relative to the radial axis by an angle θ , the Sommerfeld radiation condition in Eq. (27) should be modified accordingly to ensure the out-going property of the scattered waves and lack of it will result in distortions and reflections. The results in Fig. 15 and Fig. 16 confirm the effectiveness of the proposed radiation condition as a wave-pattern prediction tool for the ships travelling with very low forward speed.

In order to validate the wave patterns calculated by the proposed radiation condition at $\tau > 0.25$, we implement an upstream boundary condition of Nakos [18] for comparison. The upstream boundary condition assumes that there is no scattered wave travelling ahead of the vessel and a quiescent condition is imposed at the upstream boundary as

$$(i\omega_e - u_0 \frac{\partial}{\partial x})\varphi_j = (i\omega_e - u_0 \frac{\partial}{\partial x})^2 \varphi_j = 0 \quad (43)$$

Besides, no control surface is required in Nakos's [18] model. Fig. 17 and Fig. 18 show the diffracted and radiated wave patterns of both ship at $\tau = 0.27$. The upper half of each figure represents the wave pattern obtained from the present radiation condition, while the radiation condition in the lower half accounts for the upstream treatment given in Eq. (43). An evident difference of the wave patterns can be observed between these two radiation conditions, especially at far field close to the control surface. The satisfactory radiation condition must ensure that the normal component of the scattered waves is outgoing. The upstream treatment can only ensure that there is no wave travelling ahead of the vessel. However, due to the forward speed effect, most of the wave energy is transferred downstream. The outgoing property at downstream control surface cannot be guaranteed since that no radiation condition is imposed there. As a result, the reflected waves become very large at downstream control surface, which is shown in Fig. 17 and Fig. 18. If the control surface is placed far enough away from the centre ($dc/\lambda > 3$, as suggested by Das and Cheung [21], where dc is the distance between the control surface and the center, λ is the wave length), the reflected wave will not influence the near field wave patterns. But for the case of $\tau = 0.27$, the wave length is very large and $dc/\lambda = 1.4$ downstream, $dc/\lambda = 0.8$ sideward. Therefore, the near field wave patterns are also modified by the reflected wave from the control surface. As τ increases, the wave length becomes smaller. For the case of $\tau = 0.51$ in Fig. 19 and Fig. 20, $dc/\lambda = 4.1$ downstream, $dc/\lambda = 2.4$ sideward. Although there are some reflections from the control surface, they will not influence the near field wave patterns, as shown in Fig. 19 and Fig. 20. In the near field of the ship hulls, a very good agreement of the wave fields is obtained between these two radiation conditions. For the present radiation condition, the rotated angle θ has been calculated before we solve the boundary value problem. The corrected Sommerfeld radiation condition can ensure the outgoing property of the scattered waves. Therefore, no reflections can be found for the present model at $\tau > 0.25$. The results in Fig. 13-Fig. 20 confirm the effectiveness of the proposed radiation condition as a wave-pattern prediction tool for the ships travelling with a wide range of forward speed.

We also examine the effect of the radiation condition through the comparison study based on the wave excitation forces and the hydrodynamic coefficients at $F_n = 0.1$, as shown in Fig. 21 and Fig. 22 respectively. It can be clearly seen that at $\tau < 0.25$, the results from the upstream treatment are diverged and cannot provide a stable solutions. Even though τ is slightly greater than critical value 0.25, the near field wave pattern obtained by upstream treatment can still be influenced by the reflected waves from the control surface, which is analysed previously. This explains the discrepancies between the results obtained by two different radiation conditions at the range of $0.25 < \tau < 0.35$. When τ is greater than 0.35, these two radiation conditions can provide the identical results. For the present method, the solutions of the wave excitation forces and the hydrodynamic coefficients are quite stable in the full range of τ . It can be concluded that the proposed radiation condition can predict the hydrodynamic properties of vessels with forward speed above and below the group velocity of the scattered waves while the upstream treatment is only valid for the case of $\tau > 0.25$.

6 CONCLUSIONS

In this paper, we develop a boundary element program based on 3-D Rankine source method to investigate the ship-to-ship with forward speed problem. A new radiation condition, which takes Doppler shift into account, is imposed on the control surface to complete the boundary value problem. This new method is applicable to forward speeds above and below the critical frequency $\tau = 0.25$.

The present method was verified through two pairs of models. The computed dynamic responses of both models in heave and pitch motions show a good agreement with the published experimental results. However, the prediction of roll motion is full of challenges due to the inviscid assumption in the potential flow theory. The contribution of the radiation component is small, especially for the smaller ship with large amplitude of roll motion which violates the present linear assumption. In order to improve the accuracy of the prediction, a roll damping coefficient should be applied in the motion equation to avoid the unrealistic roll motions. Unfortunately, this damping coefficient could not be determined without model test results. A future study based on CFD solutions should be carried out. We also find that the hydrodynamic interaction has much greater influence on the motions of the smaller ship.

We examined the proposed radiation condition and the effect of forward speed through a series of numerical experiments involving two ships with a wide range of forward speed in head seas. The forward speed introduces the Doppler shift which modifies the length of the scattered waves. The symmetrical characteristic of wave pattern produced by single ship has been modified in the presence of the other one. The comparison between the present and Sommerfeld radiation condition was made at $\tau < 0.25$, while the comparison between the present and upstream radiation treatment was made at $\tau > 0.25$. Our solution shows a better wave pattern without reflections from the truncated control surface, which confirms the effectiveness of the proposed radiation condition as a wave-pattern prediction tool for the ships travelling with a wide range of forward speed.

7 ACKNOWLEDGMENTS

The present work is mainly funded by Lloyd's Register. Authors are grateful to Lloyd's Register for their support.

8 REFERENCES

- [1] Fang MC, Kim CH. Hydrodynamically coupled motions of two ships advancing in oblique waves. *Journal of Ship Research*. 1986;30:159-71.
- [2] Kashiwagi M. Heave and pitch motions of a catamaran advancing in waves. In: Yokohama, editor. *Proc of 2nd International Conference on Fast Sea Transportation* 1993. p. 643-55.
- [3] Iwashita H, Kataoka S. 3-D analysis of the hydrodynamic interaction between steady and unsteady flows for a catamaran. *Proceedings of Korea and Japan Joint Workshop* 1996. p. 1-9.
- [4] Chen GR, Fang MC. Hydrodynamic interactions between two ships advancing in waves. *Ocean Engineering*. 2001;28:1053-78.
- [5] Li L. Numerical seakeeping predictions of shallow water effect on two ship interactions in waves: Dalhousie University; 2001.
- [6] McTaggart K, Cumming D, Hsiung CC, Li L. Seakeeping of two ships in close proximity. *Ocean Engineering*. 2003;30:1051-63.
- [7] Li L. Numerical seakeeping simulation of model test condition for two-ship interaction in waves. *Proceedings of the 26th International Conference on Offshore Mechanics and Arctic Engineering*. San Diego, California, USA 2007. p. OMAE2007-29328.
- [8] Ronæss M. Wave induced motions of two ships advancing on parallel course: NTNU; 2002.

- [9] Xu X, Faltinsen OM. Time domain simulation of two interacting ships advancing parallel in waves. Proceedings of the 30th International Conference on Offshore Mechanics and Arctic Engineering. Rotterdam, The Netherlands 2011. p. OMAE2011-49484.
- [10] Xu Y, Dong WC. Numerical study on wave loads and motions of two ships advancing in waves by using three-dimensional translating-pulsating source. *Acta Mechanica Sinica*. 2013;29:494-502.
- [11] Lee CH, Sclavounos PD. Removing the irregular frequencies from integral equations in wave-body interactions. *Journal of Fluid Mechanics*. 1989;207:393-418.
- [12] Nossen J, Grue J, Palm E. Wave forces on three-dimensional floating bodies with small forward speed. *Journal of Fluid Mechanics*. 1991;227:135-60.
- [13] Hess JL, Smith AMO. Calculation of nonlifting potential flow about arbitrary three-dimensional bodies. *Journal of Ship Research*. 1964;8:22-44.
- [14] Sclavounos PD, Nakos DE. Stability analysis of panel methods for free surface flows with forward speed. 17th Symposium on Naval Hydrodynamics. Den Hague, Nederland 1988.
- [15] Nakos DE, Sclavounos PD. Steady and unsteady ship wave patterns. *Journal of Fluid Mechanics*. 1990;215:263-88.
- [16] Kring DC. Time domain ship motions by a three-dimensional Rankine panel method: MIT; 1994.
- [17] Gao Z, Zou Z. A NURBS-based high-order panel method for three-dimensional radiation and diffraction problems with forward speed. *Ocean Engineering*. 2008;35:1271-82.
- [18] Nakos DE. Ship wave patterns and motions by a three dimensional Rankine panel method: MIT; 1990.
- [19] Jensen G, Mi ZX, Söding H. Rankine source methods for numerical solutions of steady wave resistance problem. Proceedings of 16th Symposium on Naval Hydrodynamics. Berkeley 1986. p. 575-82.
- [20] Das S, Cheung KF. Hydroelasticity of marine vessels advancing in a seaway. *Journal of Fluids and Structures*. 2012;34:271-90.
- [21] Das S, Cheung KF. Scattered waves and motions of marine vessels advancing in a seaway. *Wave Motion*. 2012;49:181-97.
- [22] Yuan ZM, Incecik A, Jia L. A new radiation condition for ships travelling with very low forward speed. *Ocean Engineering* 2014;88:298-309.
- [23] Becker E. Das Wellenbild einer unter der Oberfläche eines Stromes schwerer Flüssigkeit pulsierenden Quelle. *Journal of Applied Mathematics and Mechanics*. 1958;38:391-9.
- [24] Miao G-P, Liu Y-Z, Yang Q-Z, Liu Z-Y. On the 3-D pulsating source of Michell type with forward speed. *Journal of Hydrodynamics, Ser B*. 1995;2:84-95.
- [25] Yuan ZM, Incecik A. Hydrodynamic interactions between two ships travelling or stationary in shallow waters. Submitted to *Ocean Engineering*.
- [26] Prins HJ. Time domain calculations of drift forces and moments. The Netherlands: Delft University of Technology; 1995.
- [27] Bunnik T. Seakeeping calculations for ships, taking into account the non-linear steady waves. The Netherlands: Delft University of Technology; 1999.
- [28] Newman JN. Distributions of sources and normal dipoles over a quadrilateral panel. *Journal of Engineering Mathematics*. 1985;20:113-26.
- [29] Longuet-Higgins MS, Cokelet ED. The deformation of steep surface waves on water (I): A numerical method of computation. Proceedings of the Royal Society of London 1976. p. 1-26.
- [30] Xu M, Yue DKP. Computations of fully-nonlinear three-dimensional water waves. Proceedings of 19th Symposium on Naval Hydrodynamics. Seoul, Korea 1995.
- [31] Huang YF. Nonlinear ship motions by a Rankine panel method: MIT; 1997.
- [32] Tarmo S. Nonlinear components of ship wake waves. *Applied Mechanics Reviews*. 2007;60:120-38.
- [33] Xu Y, Dong W. Numerical study on wave loads and motions of two ships advancing in waves by using three-dimensional translating-pulsating source. *Acta Mechanica Sinica*. 2013;29:494-502.
- [34] Chakrabarti S. Empirical calculation of roll damping for ships and barges. *Ocean Engineering*. 2001;28:915-32.
- [35] Himeno Y. Prediction of ship roll damping-state of the art. Report No239: Department of Naval Architecture and Marine Engineering, University of Michigan; 1981.

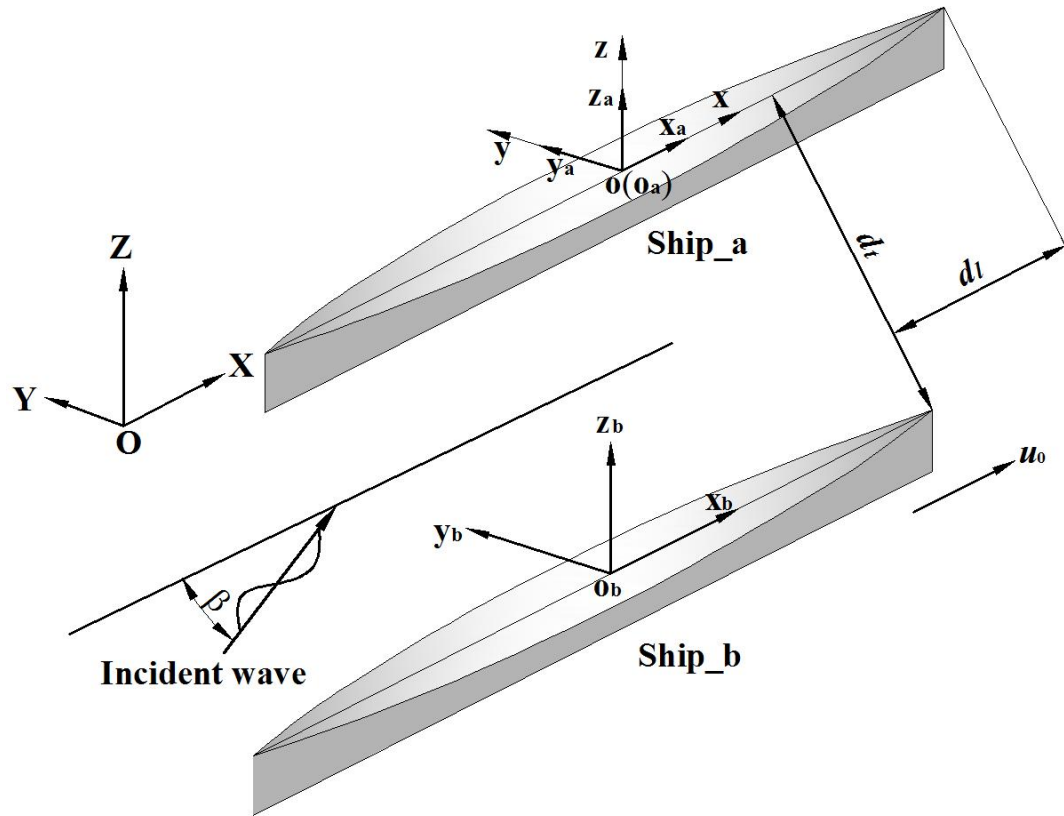


Fig. 1 An example vessels and coordinate system

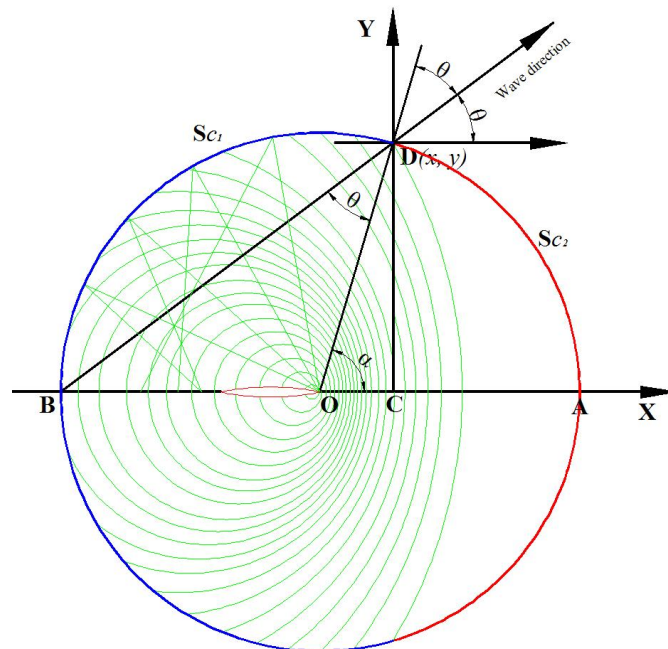


Fig. 2 Sketch of Doppler shift and radiation condition of single ship

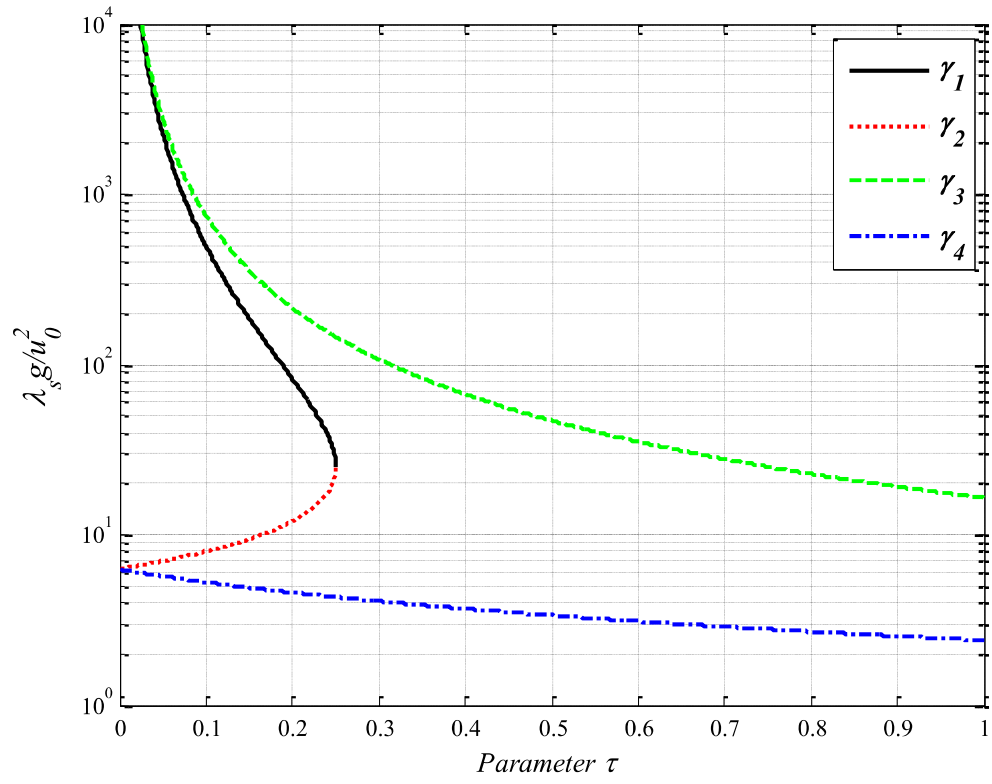


Fig. 3 The dimensionless local wave length on x-axis

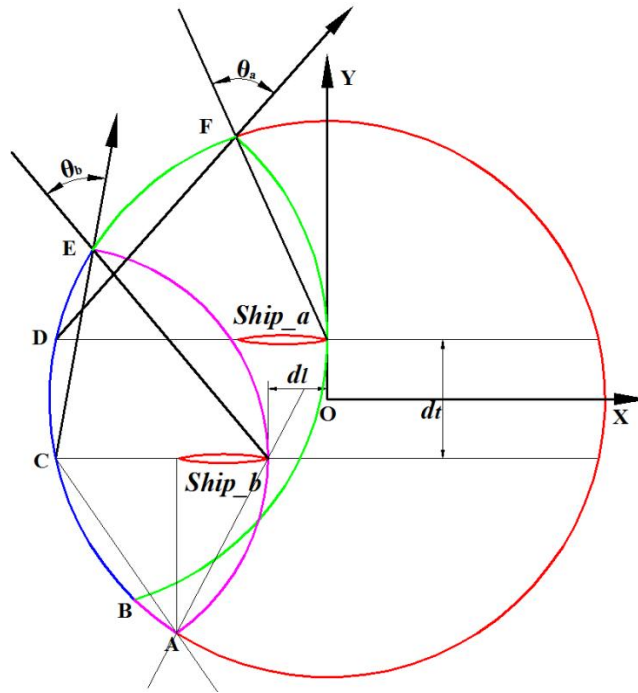


Fig. 4 Sketch of Doppler shift and radiation condition of two ships advancing in waves

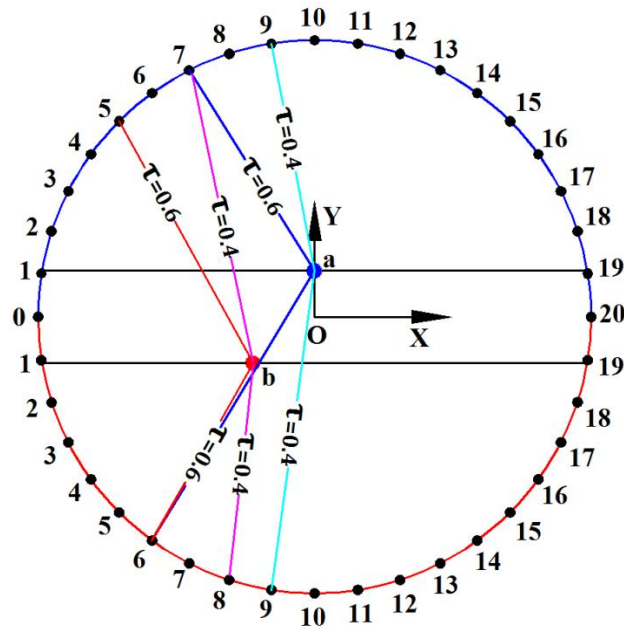


Fig. 5 Doppler shift of two translating and oscillating sources with forward speed

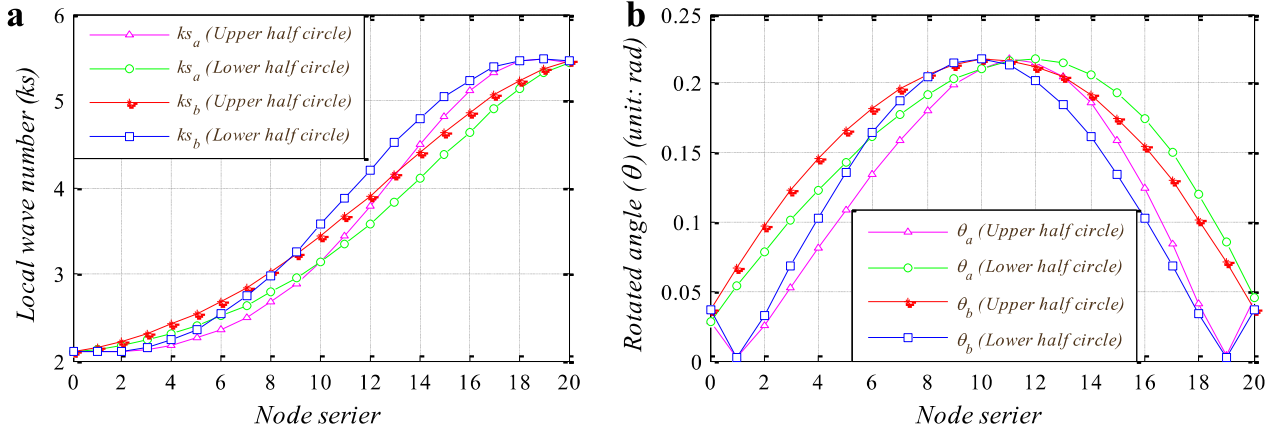


Fig. 6 Results at $\tau=0.2$. (a) Local wave number; (b) Rotated angle.

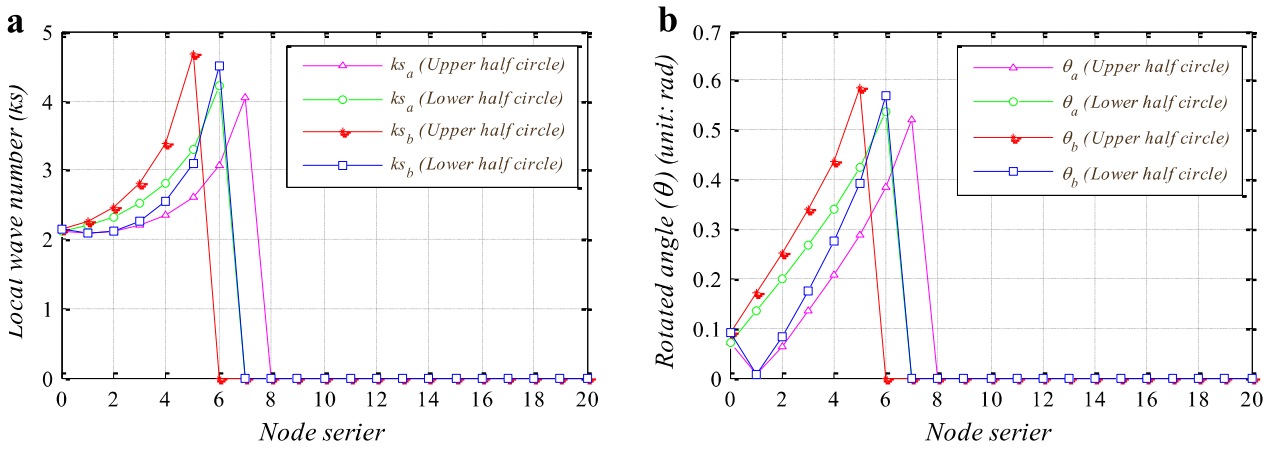


Fig. 7 Results at $\tau=0.6$. (a) Local wave number; (b) Rotated angle.

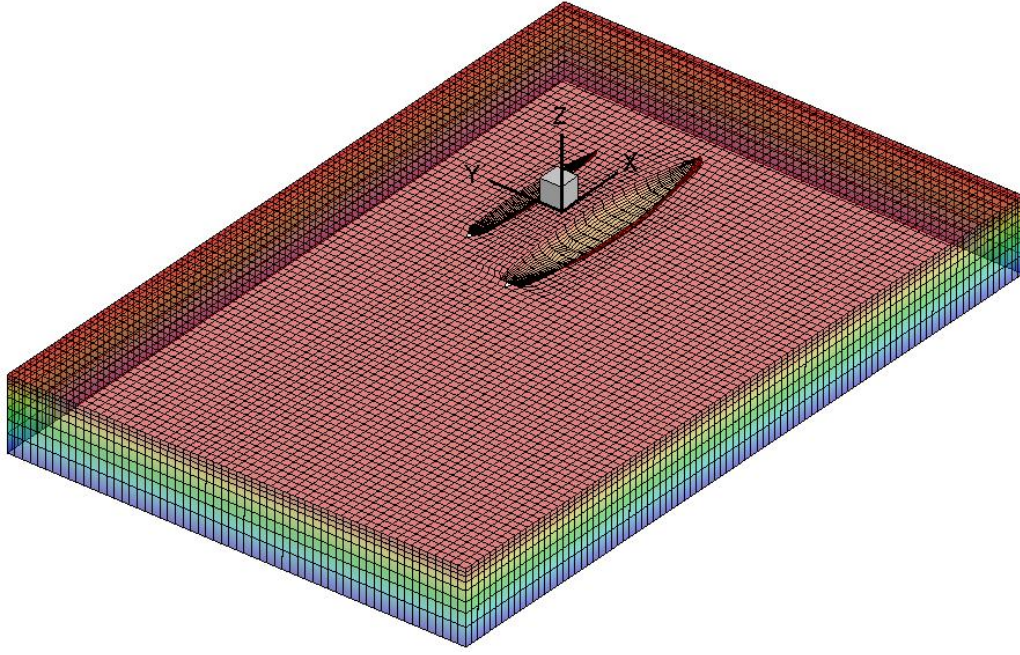
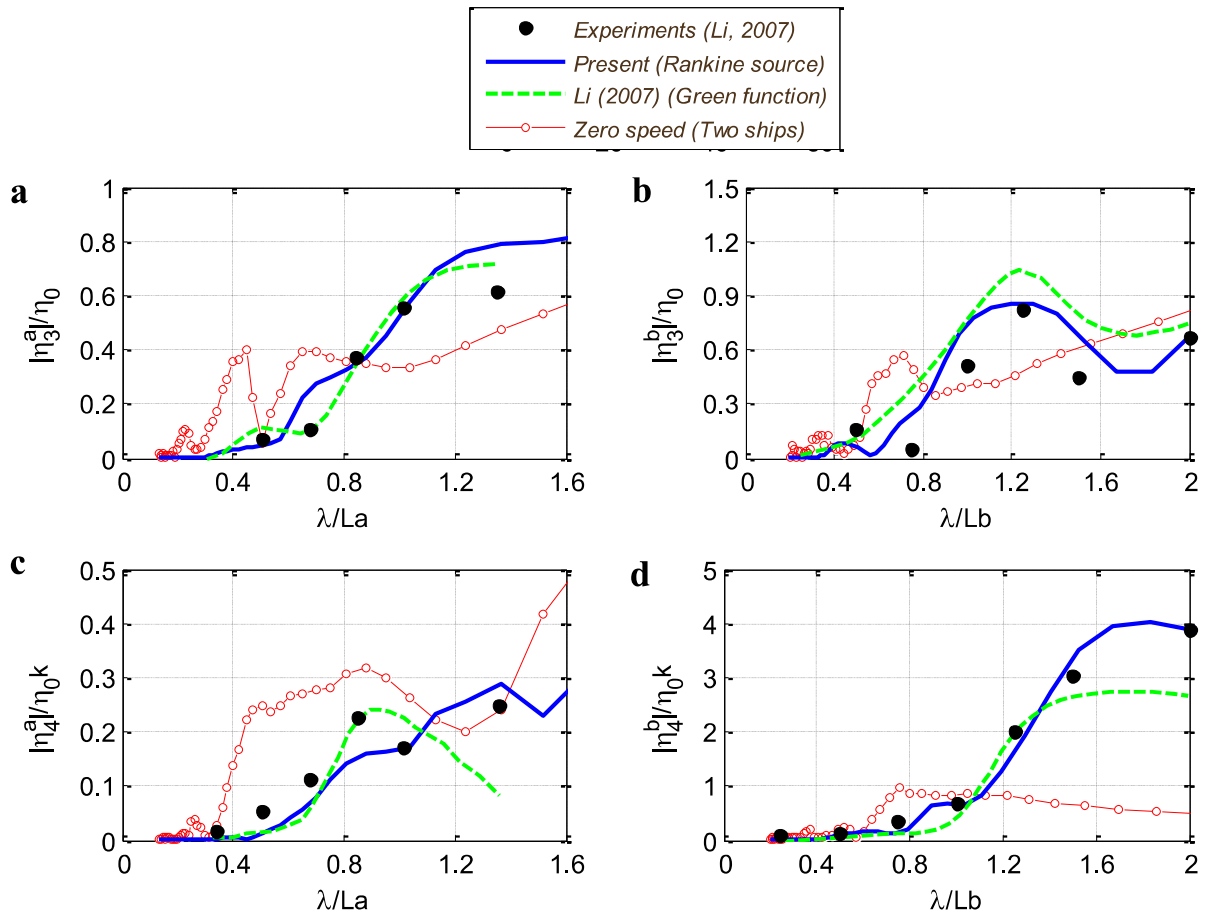


Fig. 8 Computational domain of Model 1



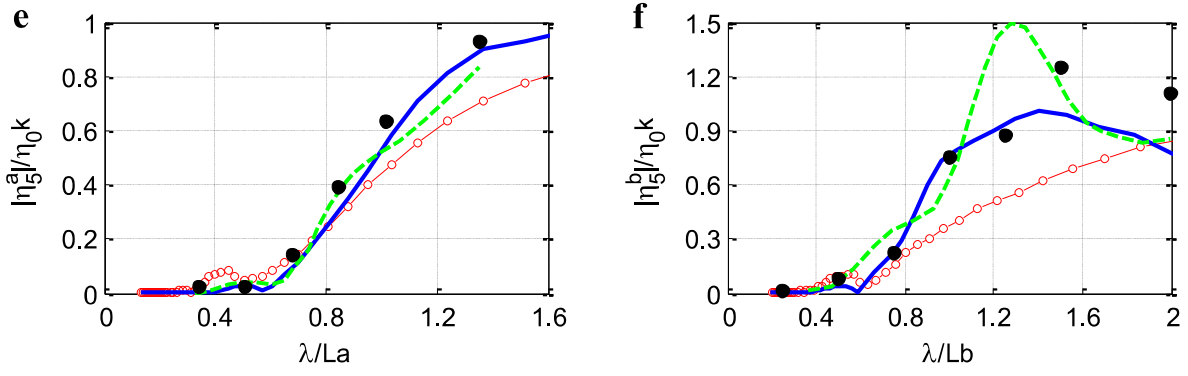


Fig. 9 Response amplitude operators of two ships at $F_n=0.15$. (a) Heave of Ship_a; (b) Heave of Ship_b; (c) Roll of Ship_a; (d) Roll of Ship_b; (e) Pitch of Ship_a; (f) Pitch of Ship_b.

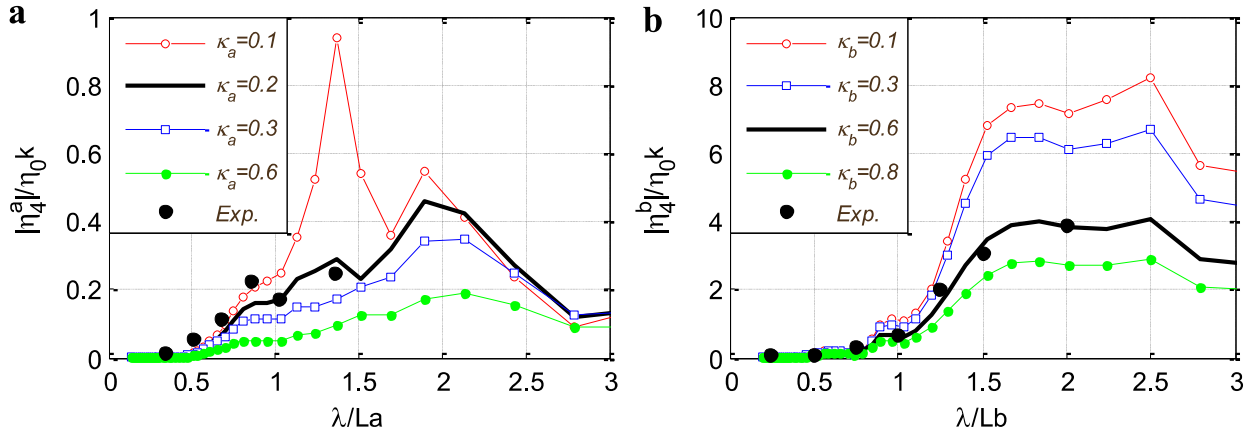


Fig. 10 Roll motion amplitudes at different damping coefficients. (a) Ship_a; (b) Ship_b.

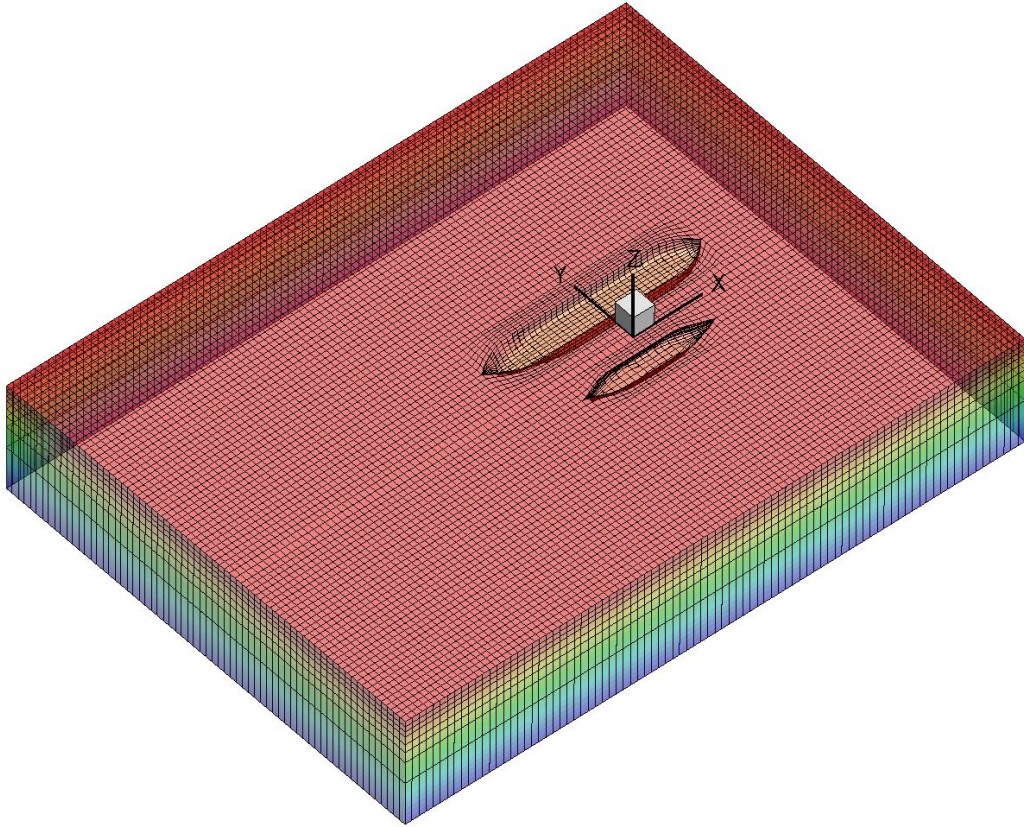


Fig. 11 Computational domain of Model 2

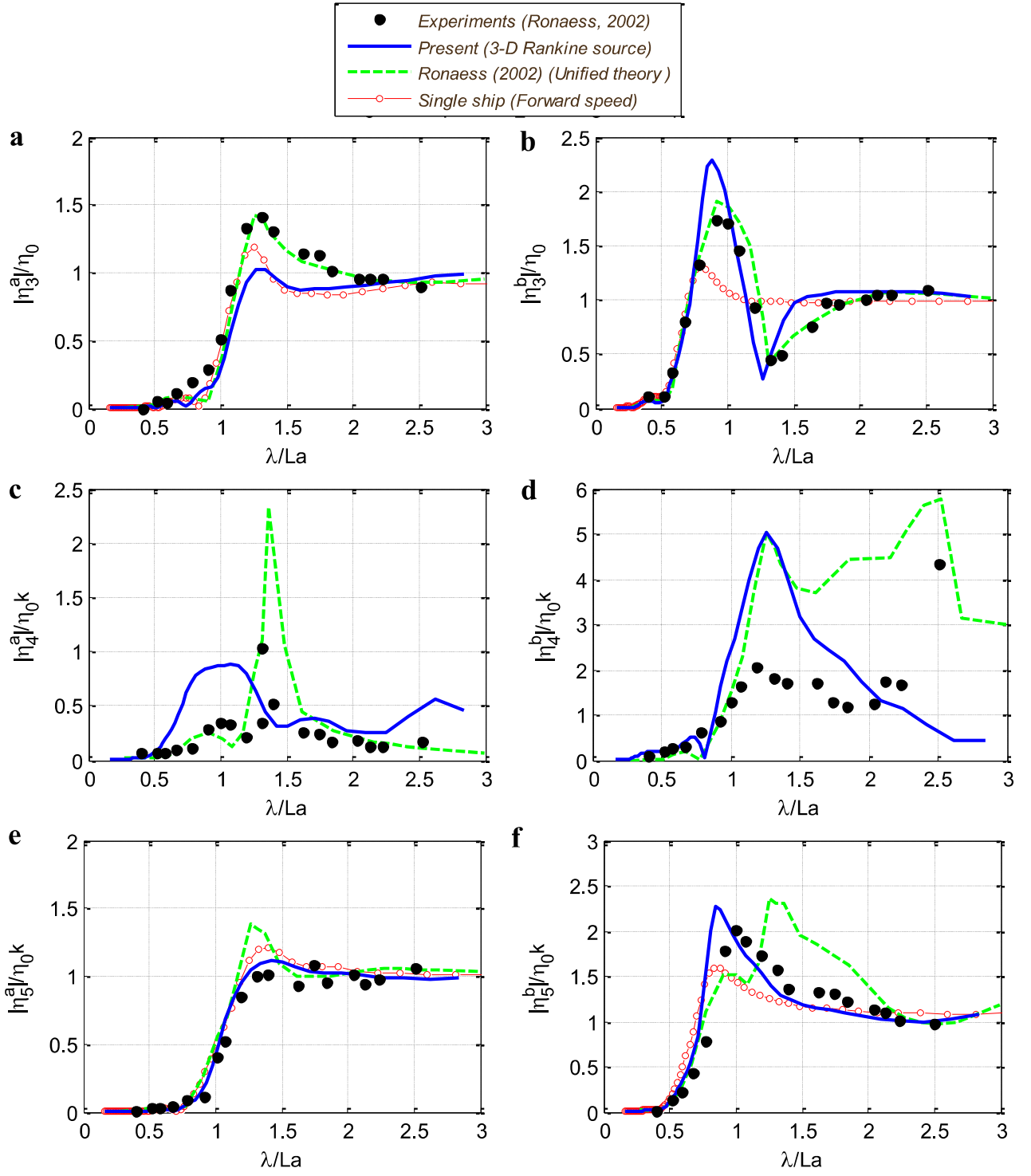


Fig. 12 Response amplitude operators of two ships at $F_n=0.15$. (a) Heave of ship_a; (b) Heave of Ship_b; (c) Roll of ship_a; (d) Roll of Ship_b; (e) Pitch of ship_a; (f) Pitch of Ship_b.

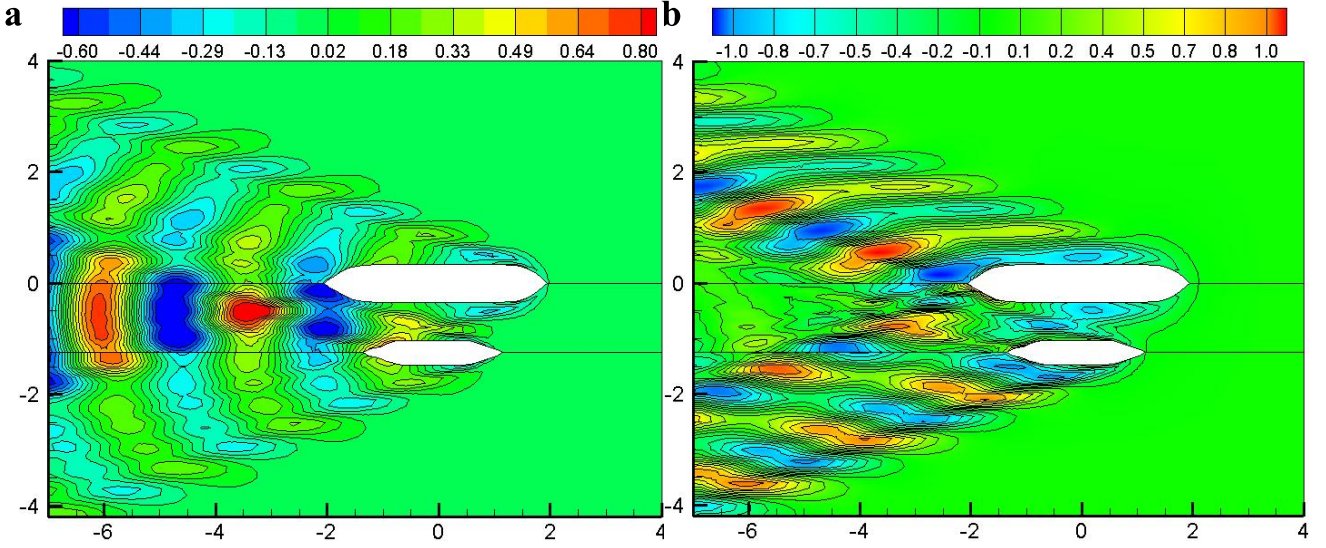


Fig. 13 Wave patterns of two ships in head seas: $\lambda/L_b=1.08$, $F_n=0.25$, $\tau=1.35$. (a) Real part of diffracted waves; (b) Real part of radiated waves for unit heave motion of both ships.

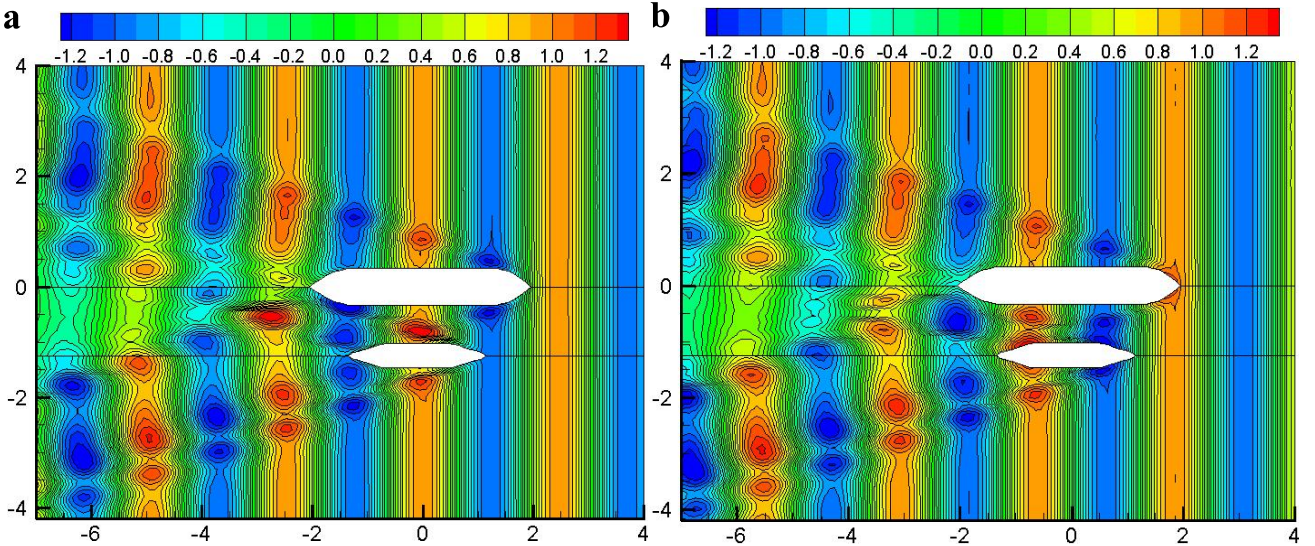


Fig. 14 Total wave elevation on the free surface of two ships in head seas: $\lambda/L_b=1.08$, $F_n=0.25$, $\tau=1.35$. (a) Real part; (b) Imaginary part.

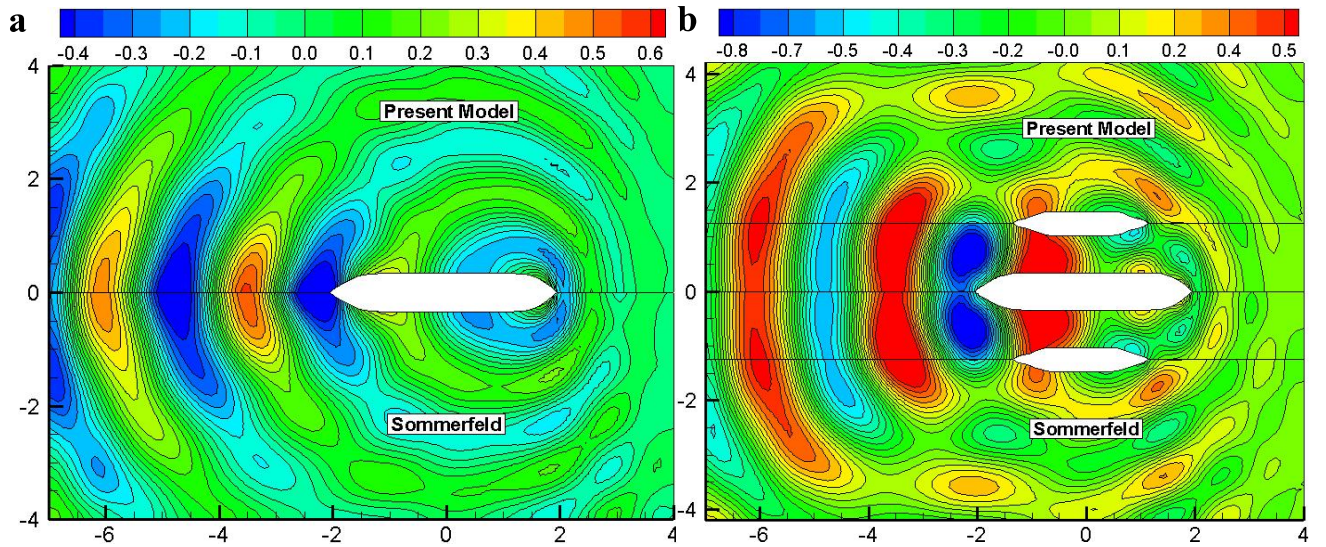


Fig. 15 Real part of diffracted waves of two ships in head seas by using Sommerfeld and present radiation condition: $\lambda/L_b=1.08$, $F_n=0.05$, $\tau=0.2$. (a) Wave pattern in the portside of Ship_a; (b) Wave pattern in the starboard of Ship_a.

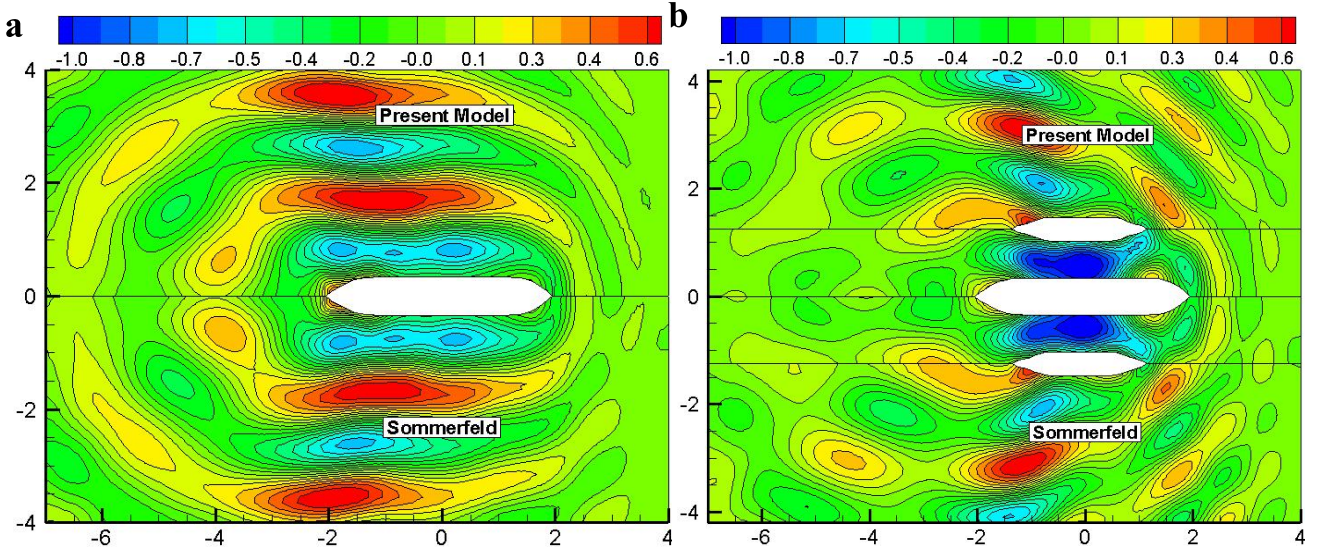


Fig. 16 Real part of radiated waves of two ships in head seas by using Sommerfeld and present radiation condition: $\lambda/L_b=1.08$, $F_n=0.05$, $\tau=0.2$. (a) Wave pattern in the portside of Ship_a; (b) Wave pattern in the starboard of Ship_a.

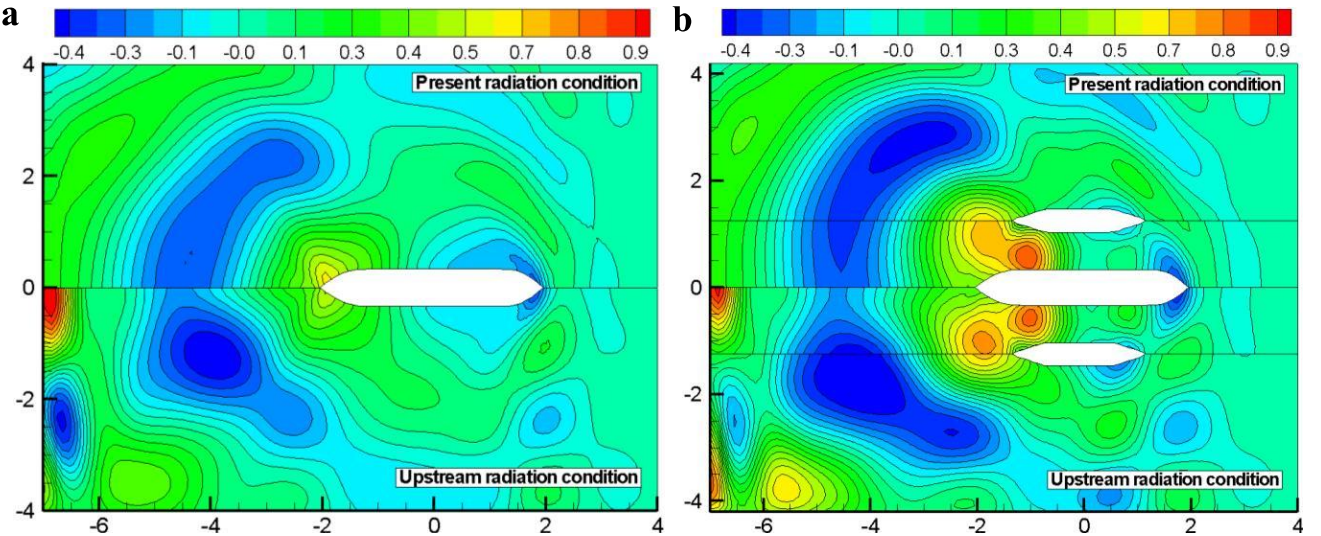


Fig. 17 Real part of diffracted waves of two ships in head seas by using upstream boundary condition of Nakos [18] and present radiation condition: $\lambda/L_b=2.15$, $F_n=0.1$, $\tau=0.27$. (a) Wave pattern in the portside of Ship_a; (b) Wave pattern in the starboard of Ship_a.

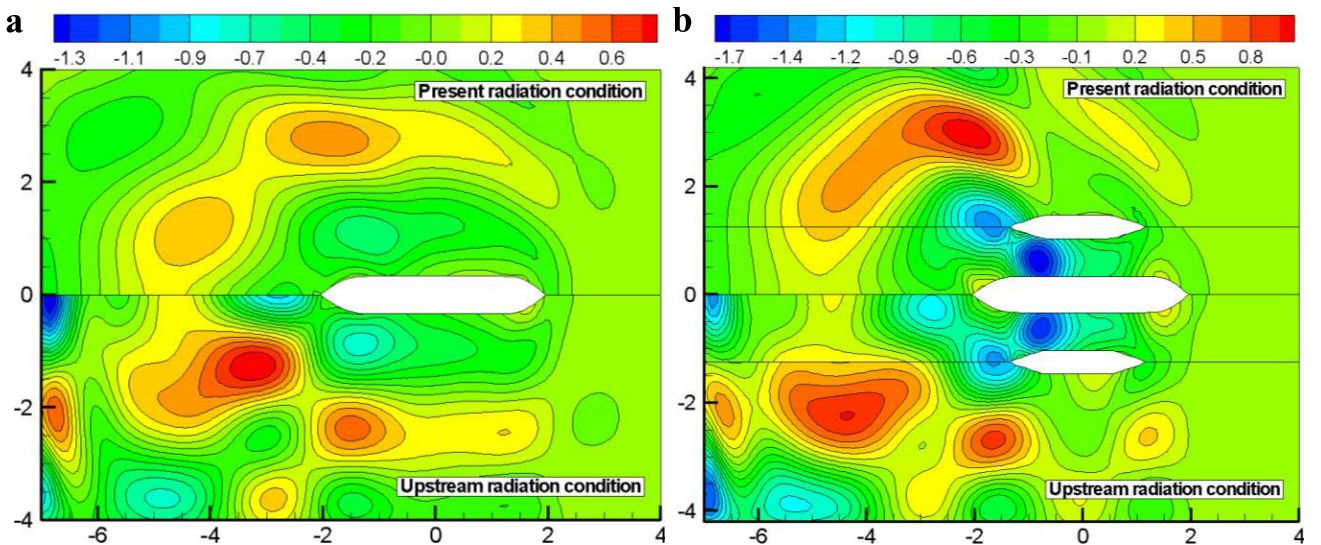


Fig. 18 Real part of radiated waves of two ships in head seas by using upstream boundary condition of Nakos [18] and present radiation condition: $\lambda/L_b=2.15$, $F_n=0.1$, $\tau=0.27$. (a) Wave pattern in the portside of Ship_a; (b) Wave pattern in the starboard of Ship_a.

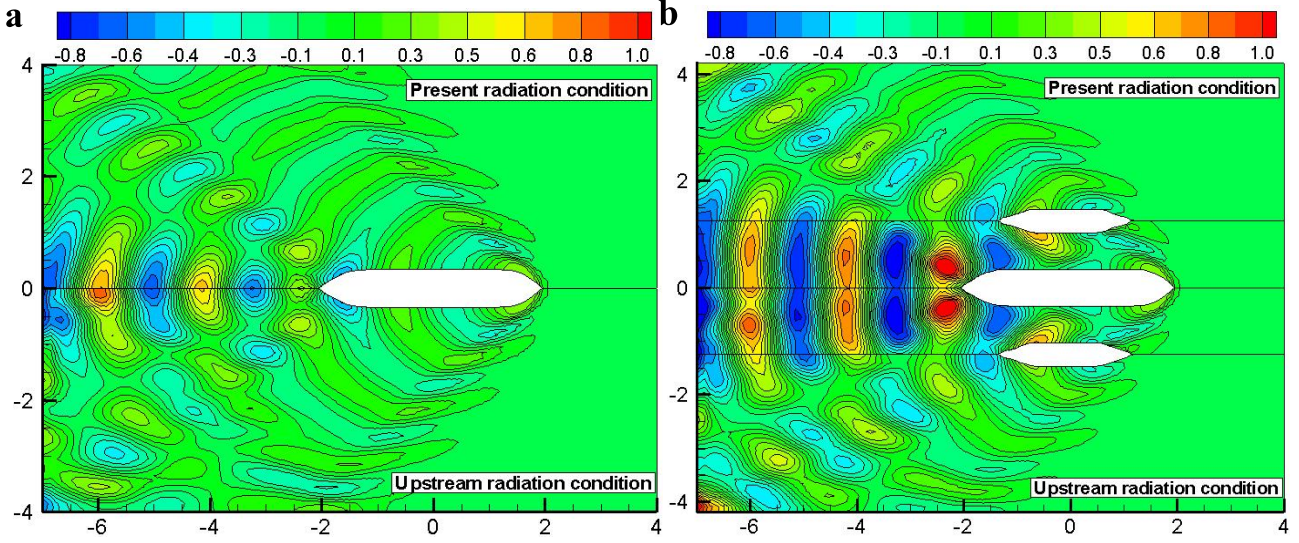


Fig. 19 Real part of diffracted waves of two ships in head seas by using upstream boundary condition of Nakos [18] and present radiation condition: $\lambda/L_b=0.75$, $F_n=0.1$, $\tau=0.51$. (a) Wave pattern in the portside of Ship_a; (b) Wave pattern in the starboard of Ship_a.

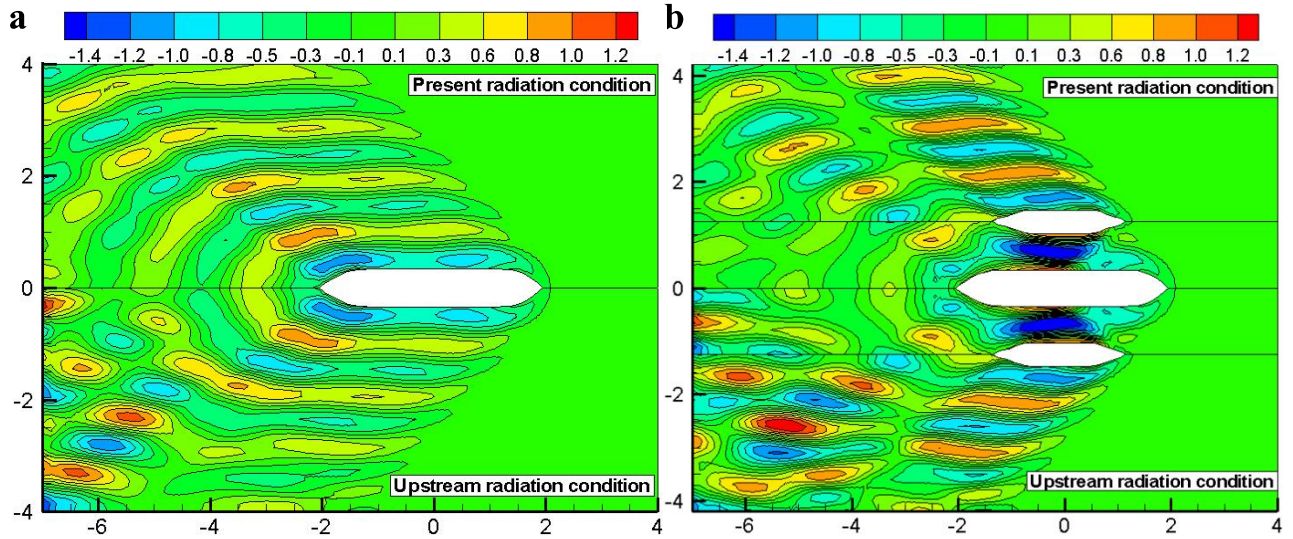


Fig. 20 Real part of radiated waves of two ships in head seas by using upstream boundary condition of Nakos [18] and present radiation condition: $\lambda/L_b=0.75$, $F_n=0.1$, $\tau=0.51$. (a) Wave pattern in the portside of Ship_a; (b) Wave pattern in the starboard of Ship_a.

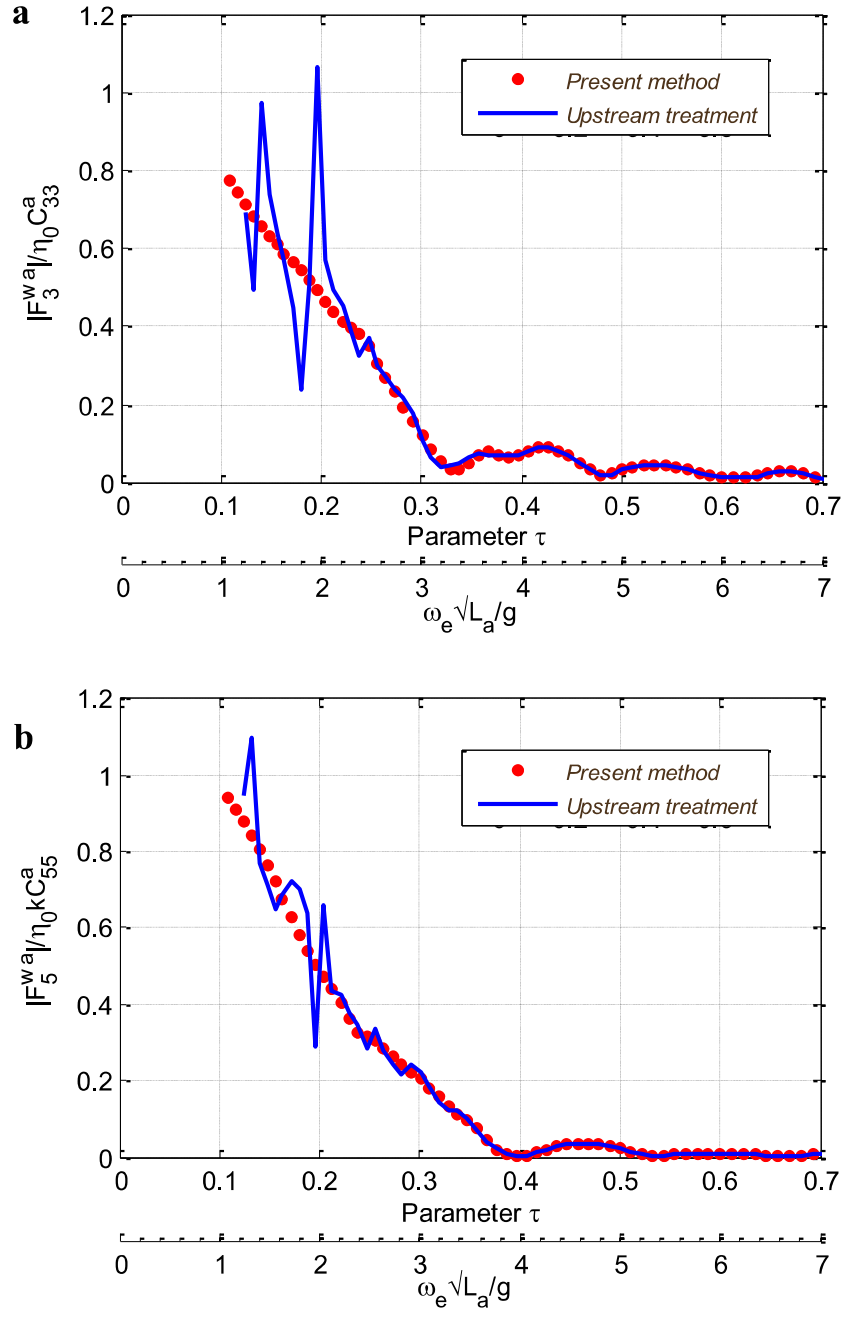


Fig. 21 Wave excitation forces on Ship_a by using upstream boundary condition of Nakos [18] and proposed radiation condition at $F_n=0.1$. (a) Heave; (b) Pitch.

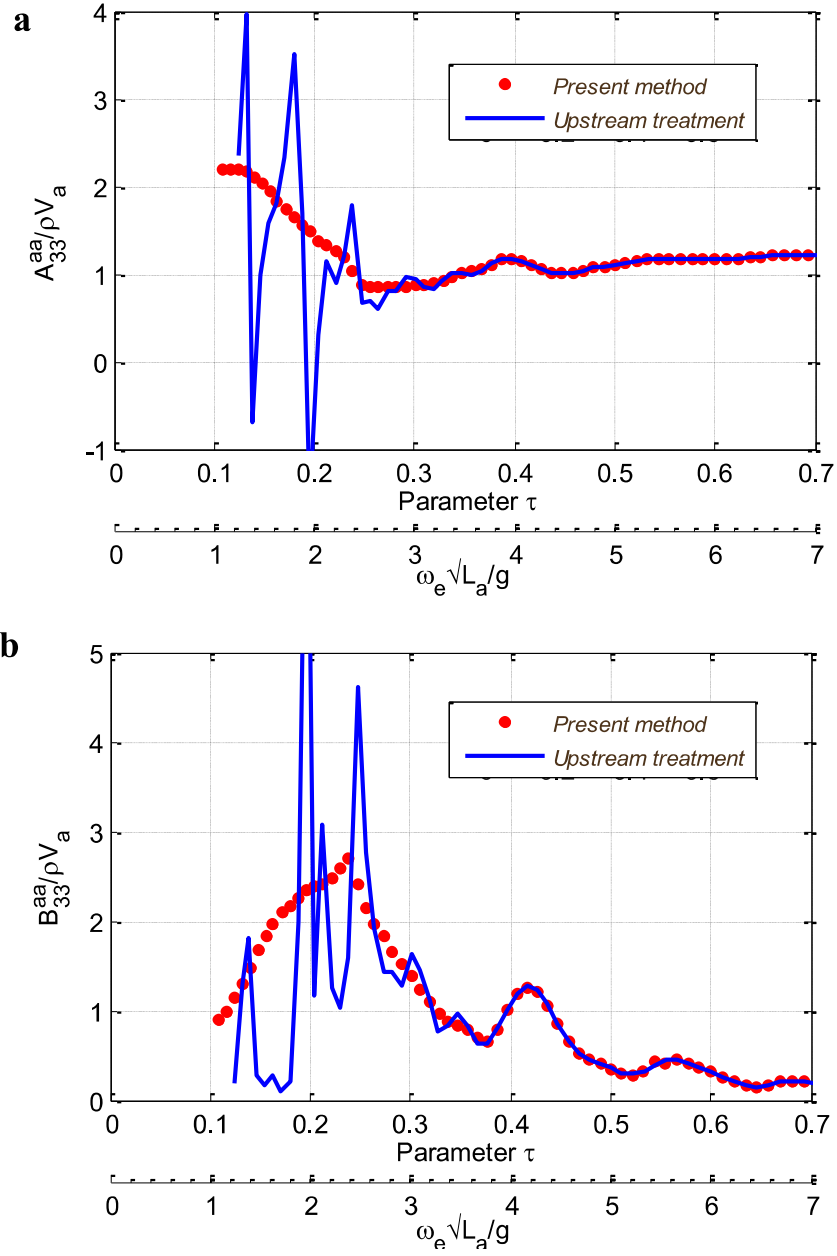


Fig. 22 Hydrodynamic coefficients by using upstream boundary condition of Nakos [18] and proposed radiation condition at $F_n=0.1$. (a) Heave added mass of Ship_a induced by heave motion of Ship_a itself; (b) Heave damping of Ship_a induced by heave motion of Ship_a itself.

Table 1
Main particulars of supply ship and frigate [5]

	<i>Supply ship</i>	<i>Frigate</i>
Length between perpendicular	$L_a=180\text{ m}$	$L_b=122\text{ m}$
Breadth	$B_a=30.633\text{ m}$	$B_b=14.78\text{ m}$
Draught	$T_a=8.5\text{ m}$	$T_b=4.5\text{ m}$
Displacement	$V_a=28223.3\text{ t}$	$V_b=4023.7\text{ t}$
Block coefficient	$C_B^a=0.588$	$C_B^b=0.484$
Longitudinal CoG (rel. midship)	$X_G^a=-1.688\text{ m}$	$X_G^b=3.284\text{ m}$
Vertical CoG (rel. calm waterline)	$Z_G^a=3.925\text{ m}$	$Z_G^b=2.049\text{ m}$
Radius of inertia for roll	$r_{44}^a=8.047\text{ m}$	$r_{44}^b=4.921\text{ m}$
Radius of inertia for pitch	$r_{55}^a=45\text{ m}$	$r_{55}^b=30.5\text{ m}$
Radius of inertia for yaw	$r_{66}^a=45\text{ m}$	$r_{66}^b=30.5\text{ m}$

Table 2
Main particulars of tanker and LNG ship [8]

	<i>Tanker</i>	<i>LNG ship</i>
Length between perpendicular	$L_a=3.76\text{ m}$	$L_b=2.28\text{ m}$
Breadth	$B_a=0.625\text{ m}$	$B_b=0.387\text{ m}$
Draught	$T_a=0.232\text{ m}$	$T_b=0.124\text{ m}$
Displacement	$V_a=0.4355\text{ t}$	$V_b=0.074\text{ t}$
Block coefficient	$C_B^a=0.83$	$C_B^b=0.68$
Water plane area coefficient	$C_w^a=0.90$	$C_w^b=0.79$
Longitudinal CoG (rel. midship)	$X_G^a=0.086\text{ m}$	$X_G^b=-0.01\text{ m}$
Vertical CoG (rel. calm waterline)	$Z_G^a=-0.052\text{ m}$	$Z_G^b=0.012\text{ m}$
Radius of inertia for roll	$r_{44}^a=0.175\text{ m}$	$r_{44}^b=0.103\text{ m}$
Radius of inertia for pitch	$r_{55}^a=1.008\text{ m}$	$r_{55}^b=0.604\text{ m}$
Radius of inertia for yaw	$r_{66}^a=1.008\text{ m}$	$r_{66}^b=0.604\text{ m}$

Table 3
Corrections for model set-up of Ship_b, non-dimensionalized using ρ , V_b , L_b , g and A_{wb} [8]

Component, $i\ j$	33	55	35, 53
Additional inertia, I_{ij}	1.6E-01	5.5E-02	-7.2E-04
Additional damping, B_{ij}	5.2E-03	1.6E-03	-2.6E-03
Additional restoring, C_{ij}	4.8E-04	1.5E-04	-2.1E-06